Quantification of Bioirrigation using Image Analysis

by

SIVAPRIYA KAZA

(Under the Direction of Suchendra M. Bhandarkar)

ABSTRACT

The presence of benthic macrofauna affects many sediment characteristics, including the structure of the sediment matrix and the transport of dissolved chemical constituents and their exchange between the benthos and the overlying water. To quantify the advective flow in the subsurface induced by benthic macrofauna as a series of high-resolution images from an experiment with an acrylic antfarm were used, where the fluorescent tracer fluorescein was added and its distribution in the sediment – caused by pumping of the arenicolid worm - was captured. Horn-Schunck, Lucas-Kanade, Cross-Correlation + Lucas-Kanade and Edge tracking methods are used to obtain the optical flow from sequence of images. The optical flow directions and magnitude obtained using the above methods are compared to the flow direction magnitude reported in literature.

INDEX WORDS: Horn-Schunck, Lucas-Kanade, edge tracking, Bio-irrigation, advection

Quantification of Bioirrigation using Image Analysis

by

SIVAPRIYA KAZA

MSAI, UNIVERSITY OF GEORGIA, 2012

B.Tech, Jawaharlal Nehru Technological University, India, 2009

A Thesis Submitted to the Graduate Faculty of The University of Georgia in Partial Fulfillment of the Requirements for the Degree

MASTER OF SCIENCE

ATHENS, GEORGIA

2012

Quantification of Bioirrigation using Image Analysis

by

SIVAPRIYA KAZA

Major Professor:	Suchendra M. Bhandarkar Christof Meile
Committee:	Walter D. Potter

Electronic Version Approved:

Maureen Grasso
Dean of the Graduate School
The University of Georgia
December 2012

DEDICATION

To mom

ACKNOWLEDGEMENTS

I would like to express the deepest appreciation to Dr.Christof Meile for giving me an opportunity to be the part of his research (and the coolest lab); without his help I wouldn't have crossed the finished line for both Graduate School and this Thesis. I am also very grateful to my advisor, Dr. Suchendra Bhandarkar, and to Dr. Don Potter. I am also thankful to Dr. Waldbusser for providing the data set I worked with. I would also like to thank Ravi Kari, Srikanth Kari, Lalitha Dandipali, Priyanka Shakamuri, Swetha Pandithi and Chaitanya Guttula who have made my stay as exciting as can be. Finally I would like to thank my parents for supporting me.

TABLE OF CONTENTS

LIST OF FIGURES

- I - the intensity of the image
- I_x - derivative of intensity in x direction
- I_y – derivative of intensity in y direction
- I_t – derivative of intensity with respect to time
- u – velocity in X direction
- v – velocity in Y-direction
- C – concentration
- D^*- diffusion dispersion tensor
- ϕ - porosity
- D^m - molecular diffusion coefficient,
- δ_{ij} - Kronecker symbol (1 if i=j, 0 else),
- α_L (m) – longitudinal dispersivity
- α_T (m) - transverse dispersivity
- α- weighting factor
- var - mean variation in velocity
- k – number of pixels in a window
- $(\Delta x, \Delta y)$ - shift of intensity in x and y directions respectively
- (xi, yi) – pixel location
- W – window size
- (λ_1, λ_2) – eigenvalues
- (m, n) - number of pixels moved in the X and Y directions respectively.
- (u_{true}, u_{true}) – true velocities
- ε_{magn} – magnitude error
- ε_{ang} – angular error
- ε_{mperc} – mean percentage error
- ε_{rms} – image reconstruction error
- ε_{cp}- cross product error
- $\varepsilon_{penalty}$ – penalty error
- ε_{ep}- endpoint error
- $(\lambda_{min}, \lambda_{max})$ - minimum and maximum eigen values
- N - normalization factor
- wt- weight used for incorporating incompressibility condition

CHAPTER 1

INTRODUCTION

Benthic infauna mix marine sediments and cause transport of chemicals dissolved in sediment porewater (e.g., Shull, et al. 2009). Burrowing organisms maintain ventilated burrows that connect to the sediment water interface to facilitate feeding and to meet their respiratory requirements for oxygen. Ventilation results in the exchange of fluid inside the burrow with overlying water, or the injection of oxidized fluids into the reducing sediment. The process of benthic organisms flushing their burrows with overlying water is called bioirrigation.

The importance of macrofauna in the field is well documented via exclusion experiments. For example, Volkenborn, et al. (2007) conducted experiments to observe the effects of bioturbating lugworms (*Arenicola marina*) on physical sediment properties and geochemical exchange processes in intertidal fine sand. A 400 m^2 intertidal and sandy shallow sub-tidal area contained plots with lugworms, as well as others in which they were excluded. After two years, a significant eight-fold decrease of sediment permeability was observed in the lugworm-excluded site. Lugworm exclusion and the associated decrease in sediment permeability resulted in an accumulation of mineralization products in the pore water. Pore-water profiles of phosphate, silicate and ammonium indicated an efficient removal of degradation products in the sediment inhabited by the lugworm. The effects of lugworm on pore-water chemistry are not limited to the areas immediately adjacent to their burrows but may affect the characteristics of the entire permeable sediment as the depletion of nutrients was evident several centimeters away from lugworm burrows. Hence, the presence of these organisms affects many sediment characteristics, including the structure of the sediment matrix and the transport of dissolved chemical constituents and their exchange between the benthos and the overlying water.

Solute transport processes can be divided into diffusion and advection. Diffusive fluxes are proportional to concentration gradients while advective transport depends on flow velocities and solute concentrations. Which transport process dominates depends on sediment composition and benthic faunal activity (Huettel 1990), with diffusion generally dominating in mud and advection in permeable sand. Because of the low permeability in muddy sediment, burrows must have at least 2 connected openings to the sediment surface to enable burrow ventilation (Meysman, et al. 2005); exchange between the oxidized burrow and the reduced sediment environment is driven by diffusion across the burrow walls. The sandy environments have higher permeability and organisms can actively pump water across blind ends of burrows into the surrounding sediment. Hence, burrows no longer need a 2-way connection to the surface. The flows that are generated within the burrow can penetrate the surrounding sediment, and advective exchange between burrow water and the pore water occurs.

To quantify advective flow in the subsurface induced by benthic macrofauna, data from an acrylic antfam was used. A thin aquarium was filled with sediment and the lugworm *Abarenicola pacifica* was placed in the sediment. The sediment was collected from the Yaquina tidal flats adjacent to the Hatfield Marine Science Center (Newport OR, USA). The images of the ant-farm setup were taken over time period of few hours. and the advective flow velocities were calculated using image processing algorithms.

Optical Flow

Image sequences contain information on the movement of objects and the underlying velocity field. Optical flow methods – techniques developed in the field of computer vision and pattern recognition and hence part of the field of Artificial Intelligence – aim at the identification of this flow field either through maximization of correlations between subsequent images or from an analysis of spatio-temporal gradients in image intensities. Applications of optical flow in the medical field include the analysis of tumor volumes and anatomical structures (Huang, et al. 2006) and measuring blood flow in arteries (Rhode, et al. 2000). In oceanography, satellite images have been used to recover ocean surface circulation from sea surface temperature fields using region matching sea surface temperature (Marcello, et al. 2007) or to characterize vortex structures from ocean color (Cohen and Herlin 1996).

Optical flow velocities can be obtained through a number of approaches that either rely on cross-correlations between images or are based on spatio-temporal gradients in image intensities (Fig. 1). In **gradient-based** methods, velocity fields are reconstructed from changes in image intensity with respect to time and space. Originally developed for rigid bodies (or advection dominated systems), the governing equations is given by

$$I_x u + I_y v + I_t = 0, \tag{1}$$

where I_x, I_y and I_t are derivatives of intensity with respect to x, y and time, and u and v are velocities in x and y directions, respectively. Since equation (1) has two unknowns, an additional constraint is required to compute the optical flow. Horn and Schunck (1981) used a global smoothness condition as an additional constraint. Lucas and Kanade (1981) assume that the displacement between two sequantial frames is approximately constant within a neighborhood of the point of consideration. For all pixels within a window optical flow equation is written by assuming constant u and v. Thus the resulting system has a larger number of equations than unknowns and is overdetermined. Weber and Malik (1995) determined the optical flow by convolving every image with different filters. The additional constraint comes from different filters at the same location. The Song and Leahy (1991) method uses divergence free constrain and incompressibility constrain to obtain the optical flow.

Optical flow velocities can also be obtained by implementing **cross correlation** techniques. In this method, features are first delineated, and identified again in the following image. The shift in the feature locations is used to then calculate the flow vector. The cross correlation technique implemented by Changming (1999) searches for locations where the correlation between the gray levels patterns between two successive frames is maximized. Quenot, et al. (1998) have implemented an orthogonal dynamic programming procedure that slices each image into two orthogonal sets of parallel overlapping strips. The displacement fields are calculated for all the strips. The second image in a time series is then reconstructed by using the displacement fields and the first image. This process is reiterated several times in a pyramidal fashion by reducing the width of strips. Jong and Joon (1998) compute the displacement with a criterion of minimum curvature differences. Optical flow can also be calculated by combining template matching with cross correlation. Yilmaz et al. (2006) describe the template matching as a brute force method of searching the image for a similar region to the object template defined in the previous frame.

CHAPTER 2

METHODS

Optical Flow and Conservation of Mass: Governing Equations

The mass conservation equation in a porous medium is given by

$$\frac{\partial \phi C}{\partial t} = \nabla.\left(\nabla(D^{*}C)\right) - \nabla(\vec{\boldsymbol{v}}\phi C), \tag{2}$$

where ϕ is porosity, *C* is concentration (in mass per volume pore fluid) and $\vec{\boldsymbol{v}} = [u, v]$ is pore fluid velocity. The diffusion-dispersion tensor D^{*} is defined as Scheidegger (1961)

$$D_{ij}{}^{*} = \phi D^{m}\delta_{ij} + (\alpha_L - \alpha_T)\frac{v_i v_j}{|v|} + \alpha_T|\vec{\boldsymbol{v}}|\delta_{ij}, \tag{3}$$

where D^{m} is the tortuosity corrected in situ molecular diffusion coefficient, δ_{ij} is the Kronecker symbol (1 if i=j, 0 otherwise), and α_L (m) and α_T (m) are longitudinal and transverse dispersivities, respectively. For uniform and time-invariant porosity, equation (2) can be written as

$$\frac{\partial C}{\partial t} = \frac{1}{\phi}\ \nabla.\left(\nabla(D^{*}C)\right) - \nabla(\vec{v}C) \tag{4}$$

and recast as

$$\frac{\partial C}{\partial t} - \frac{1}{\phi}\nabla.\left(\nabla(D^{*}C)\right) + C\left(\frac{\partial u}{\partial x} + \frac{\partial v}{\partial y}\right) + u\left(\frac{\partial C}{\partial x}\right) + v\left(\frac{\partial C}{\partial y}\right) = 0. \tag{5}$$

If the image intensity *I* is proportional to the solute concentration *C*, comparison of equations (1) and (5) gives:

$$I_x u = u\left(\frac{\partial C}{\partial x}\right), \tag{6}$$

$$I_y v = v\left(\frac{\partial C}{\partial y}\right), \tag{7}$$

$$I_t = \frac{\partial C}{\partial t} - \frac{1}{\phi}\nabla.\left(\nabla(D^*C)\right) + C\left(\frac{\partial u}{\partial x} + \frac{\partial v}{\partial y}\right) \tag{8}$$

Since water is incompressible, the term $\left(\frac{\partial u}{\partial x} + \frac{\partial v}{\partial y}\right)$ is 0.

To distinguish the actual time derivative of image intensities from the expression on the right hand side of equation 8, the latter will be identified as I_t'. With that, well-established optical flow methods can be used to identify flow dynamics underlying mass conservation equations. However, as the diffusion/dispersion term (equation 3) depends on flow velocities, optical flow velocities are calculated iteratively, e.g. starting with $\vec{\boldsymbol{v}} = 0$, and subsequently updating the dispersion tensor. Horn-Schunck, Lucas-Kanade, cross-correlation combined with Lucas-Kanade and feature tracking approaches are implemented as described below.

Flow quantification

Horn-Schunck (HS): In the HS approach (Horn and Schunck 1981), a smoothness constraint is applied by limiting the difference between the flow velocity at a point and the average velocity over a small neighborhood containing the point. This can also be done by minimizing the sum of the squares of the Laplacians of the x and y components of the flow, defined as

$$\nabla^2 q = \frac{\partial^2 q}{\partial x^2} + \frac{\partial^2 q}{\partial y^2} \approx 3(\bar{q} - q) \tag{9}$$

where $q = u, v$. The local averages $\bar{q}$ are computed as

$$\bar{q} = \frac{1}{6}\{q_{i-1,j,k} + q_{i,j+1,k} + q_{i+1,j,k} + q_{i,j-1,k}\} + \frac{1}{12}\{q_{i-1,j-1,k} + q_{i-1,j+1,k} + q_{i+1,j+1,k} + q_{i+1,j-1,k}\} \tag{10}$$

The total error ε^2 of the optical flow and the smoothness equations is given by

$$\varepsilon^2 = (\alpha^2\varepsilon_c^2 + \varepsilon_b^2) \tag{11}$$

where α^2 is a weighting factor that balances quantization error, noise and smoothness of the solution. ε_b and ε_c^2 are defined as

$$\varepsilon_b = I_x u + I_y v + I_t' \tag{12}$$

and

$$\varepsilon_c^2 = \frac{\partial^2 u}{\partial x^2} + \frac{\partial^2 u}{\partial y^2} + \frac{\partial^2 v}{\partial x^2} + \frac{\partial^2 v}{\partial y^2} \tag{13}$$

u and v are obtained by minimizing ε^2, i.e. $0 = \frac{\partial \varepsilon^2}{\partial u}$, $0 = \frac{\partial \varepsilon^2}{\partial v}$. Solving for u and v we find that

$$\left(\alpha^2 + I_x^2 + I_y^2\right)(u - \bar{u}) = \ -I_x\left(I_x \bar{u} + I_y \bar{v} + I_t'\right) \tag{14}$$

$$\left(\alpha^2 + I_x^2 + I_y^2\right)(v - \bar{v}) = \ -I_y\left(I_x \bar{u} + I_y \bar{v} + I_t'\right) \tag{15}$$

It would be costly to solve these equations simultaneously, since in the corresponding matrix the number of rows and columns is twice the number of pixels in the image. Therefore, Horn and Schunck (1981) presented an iterative method in which a new set of velocity estimates is computed from the estimated derivatives and the average of the previous velocity estimates.

$$u^{k+1} = u^k - I_x\left(\frac{I_x \bar{u}^k + I_y \bar{v}^k + I_t'}{\alpha^2 + I_x^2 + I_y^2}\right) \tag{16}$$

$$v^{k+1} = v^k - I_y\left(\frac{I_x \bar{u}^k + I_y \bar{v}^k + I_t'}{\alpha^2 + I_x^2 + I_y^2}\right) \tag{17}$$

. The smoothing parameter was varied from 0.001 to 0.5, and a value of 0.1 was chosen because at and below this value, the smoothing parameter has no effect on the pattern of flow field obtained.

Lucas Kanade (LK): The LK method (Lucas and Kanade 1981) assumes that the displacement between two sequential frames is uniform within the neighborhood of a pixel. With one equation at every pixel in a small window centered on the pixel of interest, the number of equations exceeds the number of unknowns. This forms an over-determined system. The LK method obtains a compromise solution by involving the weighted least squares principle. For example, for a window size of 3 (consisting of 9 pixels), the optical flow is described as

$$\begin{bmatrix} I_{x_1} & I_{y_1} \\ \vdots & \vdots \\ I_{x_9} & I_{y_9} \end{bmatrix} \begin{bmatrix} u \\ v \end{bmatrix} = \begin{bmatrix} I'_{t_1} \\ \vdots \\ I'_{t_9} \end{bmatrix} \tag{18}$$

With $A = \begin{bmatrix} I_{x_1} & I_{y_1} \\ \vdots & \vdots \\ I_{x_9} & I_{y_9} \end{bmatrix}$, $\vec{\boldsymbol{v}} = \begin{bmatrix} u \\ v \end{bmatrix}$, and $R = \begin{bmatrix} I'_{t_1} \\ \vdots \\ I'_{t_9} \end{bmatrix}$, the optical flow velocity is obtained as

$$\vec{\boldsymbol{v}} = (A^T A)^{-1} A^T R \tag{19}$$

The LK method is based on the initial assumption that the velocities in the neighborhood of a given pixel are constant. In reality this is not true. For a given image and window size, the mean variation in velocity (var) can be calculated as

$$var = \frac{\sum_{i,j}^{k}\left(\left(u_{(i,j)} - u_{(ni,nj)}\right)^2 + \left(v_{(i,j)} - v_{(ni,nj)}\right)^2\right)}{k} \tag{20}$$

where $u_{(i,j)}$ is the velocity at pixel (i,j), $u_{(ni,nj)}$ the velocity in its neighborhood, and k is number of pixels in the window. The optimal window size can thus be determined *a posteriori* by identifying *k* for which *var* is at a minimum.

Feature tracking: Optical flow is also obtained by tracking features in consecutive images. The features can be edges, corners or blobs. The feature selection is problem dependent. Kalal et al. (2010) described that the motion is the transformation that minimizes mismatch between the target template and the candidate patch. The features are located by examining the eigenvalues of the $\mathrm{A^TA}$ matrix (equation 19). Based on the magnitude of the eigenvalues the following inferences can be made based on this argument:

1. No feature point if λ_1 and $\lambda_2 \approx 0$
2. The identified feature is an edge if $\lambda_1 \approx 0$ and $\lambda_2$is positive

3. The identified feature is a corner if λ_1 and λ_2 are large positive values

The identified features are tracked using a Newton-Raphson method of minimizing the difference between the two windows (Tomasi and Kanade 1991). Windows of pixels encompassing a feature are tracked from one image to the next. The features are defined as edges and corners. A window is centered on each feature point. Another window (window2) is then identified in image 2 at the exact same location and optical flow is obtained using the Lucas Kanade approach. Then windows 1 and 2 are compared, and if they are similar the algorithm is stopped, else window 2 is moved to a new location by using the optical flow (Figure 3). The similarity is defined as the sum of square of the difference between the image intensities of the two windows.

Edge detection: The Sobel operator calculates the gradient of the image intensity at each point. At each image point, the gradient vector points in the direction of largest possible intensity increase, and the length of the gradient vector corresponds to the rate of change in that direction. The output of Sobel edge detector in a region of constant image intensity is a zero vector and at a point on an edge is a vector which points across the edge, from darker to brighter values. Kernels (*G*) are designed to respond maximally to edges running vertically (*Gy*=[1 1 1; 0 0 0; -1 -1 -1]) and horizontally (*Gx*=[-1 0 1; -1 0 1; -1 0 1]) relative to the pixel grid. The kernels can be applied separately to the input image, to produce separate measurements of the gradient component in each orientation. These can then be combined together to find the absolute magnitude of the gradient at each point and the orientation of that gradient (Ziou and Tabbone 1998).

Harris Corner detection: Harris and Mike (1988) Chris & Stephens, (1988) and Malik, et al. (2011), described the Harris corner detection method as follows:

if intensity locations shift by $(\Delta x, \Delta y)$ from a point (xi, yi) in a window W centered on(xi, yi) are given then the auto correlation function can be written as in equation (21) below.

$$c(x, y) = \sum_{w}[I(xi, yi) - I(xi + \Delta x, yi + \Delta y)]^2 \tag{21}$$

Equation (21) can be rewritten as

$$c(x, y) = [\Delta x \quad \Delta y] A \begin{bmatrix} \Delta x \\ \Delta y \end{bmatrix} \tag{22}$$

with $A = \begin{bmatrix} \sum I_x{}^2 & \sum I_x I_y \\ \sum I_y I_x & \sum I_y{}^2 \end{bmatrix}$.

The eigen values of matrix *A* can be used to analyze if a given point is corner point or not but the computation of eigenvalues is expensive. The computation of eigenvalues involve computation of a square root. Hence, $M(x, y)$, calculated in the window $w(x, y)$ centered on pixel (x, y), in equation (23) can be used as a replacement of eigen value decomposition by calculating trace $(\lambda_1 + \lambda_2)$ and determinant $(\lambda_1 \lambda_2)$ of the the matrix *A*. The pixel which has the local maxima in $M(x, y)$, is used as the corner point and the pixels that are not part of local maxima are set as zero. k is a tunable sensitivity parameter and (λ_1, λ_2) are the eigenvalues.

$$M(x, y) = \lambda_1 \lambda_2 - k(\lambda_1 + \lambda_2)^2 \tag{23}$$

Based on *M* the following inferences can be made:

1. *M* is large for a corner.
2. *M* is negative with large magnitude for an edge
3. |*M*| is small for a flat region.

Cross-Correlation + Lucas Kanade: First, the order of magnitude of the velocity field is determined a global smoothing approach (Horn and Schunck 1981), which only requires a smoothing parameter, set to a value of 0.1. This first estimate of flow magnitudes is used to establish the size of the search window in which a subimage from image 1 is to be identified in image 2. The correspondence *C* between two such windows (b_1, b_2) is quantified as

$$C = \min \sum_{m=0}^{M1} \sum_{n=0}^{N1} b_2(i+m, j+n)^2 - 2b_2(i+m, j+n)b_1(i,j) + b_1(i,j)^2 \tag{24}$$

where *M1* and *N1* denote the size of the search window and (m, n) denote number of pixels moved in the x and y directions respectively. The velocities are then computed from the optimal translocations, *u*, *v* as *u=m*dx/dt* and *v = n*dy/dt*, where *dx*, *dy* and *dt* denote pixel sizes and time between images.

Errors quantification

Error measures are used to estimate the accuracy of the optical flow fields by comparing them with known flow fields (i.e, ground truth). The following four measures were implemented:

1. Magnitude error (McCane, et al. 2001), defined as the difference in flow magnitude:
$$\varepsilon_{magn} = \sqrt{u^2 + v^2} - \sqrt{{u_{true}}^2 + {v_{true}}^2} \tag{25}$$
2. The endpoint error, defined as the distance between the end point of true and calculated velocities:
$$\varepsilon_{ep} = \sqrt{(u - u_{true})^2 + (v - v_{true})^2} \tag{26}$$
3. The relative end point error:
$$\varepsilon_{rep} = \frac{\sqrt{(u-u_{true})^2+(v-v_{true})^2}}{\sqrt{{u_{true}}^2+{v_{true}}^2}} \tag{27}$$
4. The cross product error, reflecting the area spanned by the true and reconstructed flow vectors
$$\varepsilon_{cp} = abs\left(\begin{pmatrix} u \\ v \end{pmatrix} \times \begin{pmatrix} u_{true} \\ v_{true} \end{pmatrix}\right) \tag{28}$$

Other error measure used in literature but not considered here include:

Penalty error, defined as the product of magnitude error and direction between true and calculated velocities at a given pixel:

$$\varepsilon_{penalty} = \sum_{i=1}^{M}\sum_{j=1}^{N}\left(\varepsilon_{magn_{(i,j)}} * direction_{(i,j)}\right) \tag{29}$$

Angular flow error (Galvin, et al. (1998), Baker, et al. (2007), Osa, et al. (1998) and Barron, et al. (1994)), implemented as:

$$\varepsilon_{ang} = cos^{-1}(\begin{pmatrix} u \\ v \end{pmatrix} . \begin{pmatrix} u_{true} \\ v_{true} \end{pmatrix}) \tag{30}$$

Mean percentage error (Mitchie, et al. (1987)):

$$\varepsilon_{mperc} = \frac{|\begin{pmatrix} u \\ v \end{pmatrix} - \begin{pmatrix} u_{true} \\ v_{true} \end{pmatrix}|}{|\begin{pmatrix} u_{true} \\ v_{true} \end{pmatrix}|} \tag{31}$$

.

Image reconstruction error (Mahzoun, et al. (1999) Lin et al. (1994))

$$\varepsilon_{rms} = \sqrt{\frac{\sum_x \sum_y (I(x,y,t) - I(x,y,t)')^2}{MXN}} \tag{32}$$

where *I(x,y,t)* is the original and *I(x,y,t)*$'$ the reconstructed image of size *MxN*.

Optimal Error Measure and Quality Index

If the true velocities are known, the performance of optical flow techniques can be evaluated by implementing different error measures. If the true velocities are unknown then a confidence measure is useful for detecting unreliable flow estimates. A method for the estimation of image velocity using least squares is treated as (unconstrained) optimization problem using a form known as the Rayleigh Quotient (equation 33), (Markovsky and Van Huffel 2007)

$$RQ = \frac{\left\|A^T A\vec{u}\right\|^2}{||\vec{u}||^2} \tag{33}$$

The Rayleigh Quotient of the covariance matrix $(A^T A)$ is bounded (Eriksson 1999) above and below by the maximum and minimum eigenvalue, Knyazev and Argentati, (2006).

$$\lambda_{min} \leq RQ \leq \lambda_{max}. \tag{34}$$

Knyazev and Neymeyr, (2009) and Eriksson (1999) stated that when the Rayleigh Quotient is maximum the solution points to a local minimum. Hence, the best least squares approximation to the Rayleigh Quotient is obtained at the maximum eigenvalue of $A^T A$.

The condition number, given in equation (35), is computed for each image region. A region with higher condition number indicates that this area has a reliable estimate of optical flow. The image velocity is less well constrained in the direction of the eigenvector corresponding to the smaller condition number.

$$condition\,number = \left(\frac{\lambda_{min}}{\lambda_{max}}\right)^2 \tag{35}$$

The condition number lies in the interval [0,1]. As seen in Chapter 2, areas where the eigenvalues are really small and close to each other represent the low texture regions but the condition number value is close to 1. Hence, we use the distance between the eigenvalues, to identify low and high texture regions. The distance between the eigenvalues is used to identify regions where enough information is available to make statements about the flow using the equation (36).

$$d = \left(\frac{\lambda_{maximum} - \lambda_{minimum}}{\lambda_{maximum} + \lambda_{minimum}}\right) \tag{36}$$

If the eigenvalues are small and close to each other, then distance between the eigenvalues is close to 0, indicating low texture regions.

We define a confidence measure (Q) that combines the above two measures. The pixels whose distance between two eigenvalues is less than a cutoff value of 0.05 are considered low texture regions. The confidence measure of the pixels that belong to high texture region is set equal to condition number while in low texture regions it is set to zero:

$$Q = condition\,number * \ (d > 0.05) \tag{37}$$

CHAPTER 3

DESCRIPTION OF DATA

Test Images

Before applying the algorithms on the real image data set, they were tested on the synthetic images. Comsol Multiphysics 3.5a was used to create these images with a two-dimensional model domain that mimics the ant farm setup. Pumping velocities were imposed at the burrow ending and at time zero, a tracer was added at the burrow end that corresponds to the location of the *arenicola* head. The tracer was injected at the burrow outlet for the first ten seconds. The arrow directions in Figure 4 represent the flow of the tracer and the gray scale intensities in the image denote the reflect the tracer concentration, with the sediment in black and the lighter gray scale values denoting the tracer. The images were captured at 10-second intervals for 100 seconds (Figure 4). As there is no flow inside the burrow region, the burrow is not included in the region of interest in which the velocity field is being computed and compared to the known velocities.

Real Images

As a part of collaborative NSF grant, Dr. Waldbusser set up an acrylic ant farm style aquarium measuring 22cm x 44.5cm x 2.2cm. Sediment was collected from the Yaquina tide flats adjacent to the Hatfield Marine Science Center (Newport OR, USA) in habitats where the lugworm *Abarenicola pacifica* is found. Sediment was placed in the aquarium one week prior to adding the organism. During this time a water supply was maintained and air was bubbled in the overlying water. The aquarium was maintained in the dark. Then, fluorescein was added and its distribution in the sediment – caused by pumping of the arenicolid worm - was captured as a series of high resolution images of the fluorescent flow tracer. Fluorescein was injected at a depth of 10 cm. 0.5-1 ml of 1g per liter fluorescein was added in a NaCl solution of 32 ppt. When using lower concentrations, NaCl was added to prevent ionic imbalance. At a higher concentration, the fluorescein solution has a higher density than seawater

Experiment 1: Frames were shot on 10 s intervals with a Fujifilm FinePix S5Pro model at resolution 4256 X 2848 pixels. The two dimensional RGB images of the ant farm were taken on a ten second sequence over a fifty-minute interval. All three hundred images are used to calculate the optical flow. The last image and the region of interest are shown in Figure 9.

Experiment 2: A Fuji HS20 Pro digital SLR infrared camera was mounted on a fixed mount connected to the aquarium and connected to a laptop to control the camera shutter. A Peca 914 IR filter (highpass at 700 nm) was used along with two infrared spotlights lights to provide imaging capabilities with limited light disturbance of the organism and preventing algae growth on the interior surface of the aquarium. Gray scale images were taken every 30 min for one-week intervals, with manual settings of: ISO 200, exposure 20, F-stop 3.5, white balance K4200. Figures 6-8 represent original images taken in October, November and June respectively. The region of interest of is highlighted in the red box.

Calibration: For the quantification of flow, the image data need to be translated into concentration fields because the governing equations are based on conversation of mass. For calibration, the fluorescein concentration was varied from 0.1 to 0.6 mg/L and showed a linear relationship with image intensity (Figure 10)

Region of interest: The image used for the quantification of the flow field is a cropped subset, large enough to enclose the area with visible fluorescein in the sediment, but not including the water. The reason for that is that the optical depth in the water changes, so if you have outflow from sediment to the water at the back side of the aquarium, fluorescein all the sudden becomes visible. Such a change does not indicate a change in the nature of the image per se and an adjustment to that would lead to erroneous interpretation of flow in the porous medium.

Normalization: Image intensities vary over time due to external factors like someone opening a door, which may make the images brighter. Figure (5(a)) shows 50, 75 and 90 percentile of the intensity (I50, I75 and I90), which varies from 0.12 to 0.29 over time. To account for these changes, the image intensities were normalized by multiplying the intensity at a given pixel with a ratio of normalization factor N to $I75$ of the respective image,

$$I = I*I75(\text{image})/N \qquad (38)$$

where N is set to the 75 percentile of $I75$ from an entire image sequence as the 90 percentile shows peaks in intensities between images that do not show obvious lighting effects.

CHAPTER 4

RESULTS AND DISCUSSION

Flow reconstruction on test images

To assess the performance of the algorithms used to reconstruct the flow field, simulations were first performed with a known flow field. These true velocities point radially away from the burrow opening, with the highest velocities at the injection point (Figure 11).

The flow obtained using the *Horn-Schunck* (HS) method is shown in Figure 12. The flow moves away from the burrow and spreads in outward direction. The pattern of the flow is similar to the pattern of true velocities compare Figures 11, 12 (b) and (c). However, during the time interval 10-20 seconds Figure 11a, the region closer to burrow has the flow pointing towards the burrow as opposed to pointing away from it. For the image pair denoting the (10-20) time interval, the intensity in image 1 is large when compared to intensity of image 2. Hence, the time step may be too large to calculate the velocities because the temporal resolution is poor with these steep intensity gradients

The variation in velocity vs window size shows that minimum variation in velocity is obtained at window size of 40 Figure 13. Hence, the optimal window size is set as 40. The flow obtained using the *Lucas-Kanade* (LK) method is shown in Figure 14. The velocity vectors point away from the burrow and the overall pattern of flow is similar to the true velocity pattern Figure 11. As described in Chapter 3, the optical flow velocities are calculated as the solution to a least-squares optimization problem in a window centered on the point of interest. Thus, no flow velocities are obtained within a distance half the window size from the image boundaries. This includes the region adjacent to the burrow inlet, so that the area of the main shortcoming of the Horn-Schunck method is not included. At time steps (30-40) and (80-90) seconds Figure 14-(b) and (c) though the flow is outward in direction, at locations (0.05,0) and (0.04,0) the flow converges horizontally.

The flow obtained using the *CC+LK* method is shown in Figure 15. The flow direction doesn’t follow a clear pattern and bears little to no similarities with the true velocities. Since the CC+LK method is also dependent on the Lucas-Kanade window (Chapter 3), velocities near the burrow region are not calculated.

The optical flow obtained using *edge-tracking* methods is shown in Figure 16. The velocities are obtained only in those regions with features and having a high confidence measure. Hence, interpolation of the velocities is not observed in the edge tracking method. The direction of the flow of velocities is preserved in the edge tracking method.

Error analysis and establishment of a confidence measure

For the images taken at time steps (10-20), (30-40) and (80-90) seconds, the errors vs. confidence measure graphs are shown in Figures 17, 18 and 19, respectively. These graphs are used to establish confidence measure cut-off. The flow obtained in the regions whose confidence measure is greater than cut-off value is considered as reliable flow.

As the confidence measure increased the *magnitude error* for HS, LK and edge tracking methods decreased. The CC+LK method didnot follow any pattern in magnitude error. The magnitude error obtained from HS, LK and edge tracking methods is 10 times smaller than magnitude error of the CC+LK method. The HS and edge tracking methods exhibit a similar pattern with the error dropping rapidly at a confidence measure of 0.005. The HS and edge tracking methods also have the lowest magnitude error of $2*10^{-4}$ m/s. The magnitude error for the LK method gradually decreased with increase in confidence measure. The same pattern is observed for all three-time periods shown here. Hence based on the magnitude error, a confidence measure of 0.005 can be used as cut off.

For all optical flow methods, the *cross product error* decayed as the confidence measure increased. The cross product error of the HS, LK and edge tracking methods is 10 times smaller than the cross product error of CC+LK method. The cross product error dropped significantly for all methods when the confidence measure is greater than or equal to 0.005. For a confidence measure value of 0.005, the edge-tracking method has the lowest cross product error of 10^{-9} m/s. The LK, HS and edge tracking methods exhibit similar pattern in the cross product error. Hence basing on cross product error, a confidence measure of 0.005 can be used as a cut off.

As the confidence measure increased the *endpoint error* for the HS, LK and edge tracking methods decreased. The CC+LK method didn't follow any clear pattern. The HS, LK and edge tracking methods had the lowest error when compared to the CC+LK method. For a confidence measure value of 0.005, the edge tracking and HS method had the lowest endpoint error of $2*10^{-4}$ m/s. The endpoint error for the LK method gradually decreased over time. In HS and edge-tracking methods, the end point error dropped to smaller values at confidence measure of 0.005. Hence based on endpoint error, a confidence measure value of 0.005 can be used as a cut off.

A rapid decay of the error with an increase in the confidence measure is seen in particular for cross product and end point error Figures 17, 18 and 19; in addition it should be noted that the cross product and end point errors at (80-90) seconds is 10 times lower than the corresponding errors at (10-20) and (30-40) seconds. Also, at all time intervals, the overall pattern in magnitude error, cross product error and endpoint error vs. confidence measure is similar, particularly for HS. The CC method had the largest errors and didn't show the desired error pattern with respect to the confidence measure and is therefore not used for real images. The edge tracking method has the lowest error value, which reflects the fact that it only captures flow at well-defined locations.

Flow fields within regions of high confidence value

A cut-off of 0.005 is used to filter the calculated velocities. The pattern between the errors vs. confidence measure observed in edge tracking method is similar to that using the LK method in the regions whose confidence measure greater than or equal to 0.005. Hence, the flow fields obtained in the edge –tracking method are considered reliable. The magnitude of the flow field is around 10^{-4} m/s.

HS method:

In the case of the HS method, Figure (20-(a)) the region near the burrow still has some velocities pointing towards the burrow. The flow pattern is outward in Figures (20-(b) and (c)) and is similar to the true velocity pattern found in figure (11). The magnitude of the flow field is $2*10^{-4}$m/s in Figures (20-(a) and (b)) and decreased to $0.5*10^{-4}$m/s in Figure (20-(c)). Thus, the magnitude of the flow decreases over time at the regions closer to the burrow. At different time steps, at regions away from the burrow the velocity is observed to be in the range of $0.1*10^{-4}$m/s and $2*10^{-4}$m/s.

CC+LK method:

In the CC+LK method Figures 21-(a),(b) and (c), the region with confidence measure greater than 0.005, exhibits a flow field which doesn't match the true flow pattern. Hence the CC+LK method is not used on real image data set.

LK method:

In the LK Figures 22- (b) and (c) method the region where the flow converged to a point is identified as a region with confidence measure less than 0.005 and hence is removed with HS. The magnitude of the flow field obtained from LK method exceeds that obtained with HS method. The magnitude of the flow field ranges from $1*10^{-4}$ to $3*10^{-4}$ m/s at regions near and away from the burrow as seen in Figure (22-(a),(b) and (c)). From Figures (20 and 22), the velocities obtained in the case of the HS method decayed faster when compared to those obtained via the LK methods.

Flow reconstruction on real images

Data from 3 distinct experiments (Oct 26, Nov 2 and June 28) were analyzed:

Oct 26: One time slice of the reliable flow velocities (i.e., at locations with confidence measure > 0.005) obtained by using the HS and LK methods are shown in Figures 23 and 24, respectively. The pattern in the flow fields obtained by implementing the HS and LK methods is nearly identical. The magnitude of the flow significantly decreased over time in the case of the HS but not in the case of the LK method. The flow velocities near the sediment water interface are high (about 10^{-3} cm/s) when compared to deeper in the sediment, where they reach 10^{-5} cm/s to 10^{-4} cm/s. The magnitude of the flow near the sediment water interface is. The flow velocities obtained by using edge-tracking method are shown in Figures 25, 26 and 27. The velocities are obtained only in those regions where the edges are clearly visible. The directions of the velocity vectors obtained from the edge tracking method matches those obtained using the HS and the LK and with typical velocities of approximately $2*10^{-4}$ cm/s in the sediment.

Nov 2: A snapshot of the reliable flow velocities obtained using the HS and the LK methods are shown in Figures 28, 29 and 30. The pattern of flow fields obtained by implementing the HS and the LK methods looks nearly identical. The magnitude of the flow decayed rapidly in case of the HS method when compared to the LK method. The flow velocities near the sediment water interface are high when compared to regions associated with the sediment-containing tracer. The magnitude of the flow in the sediment ranges from 10^{-6} cm/s to 10^{-4}cm/s, while near the sediment water interface it is about $2*10^{-4}$ cm/s. The flow velocities obtained by using edge tracking are shown in Figures 31, 32 and 33. The directions of the velocities are preserved in the edge tracking method, with typical velocities of approximately $2*10^{-4}$ cm/s.

June 28: The reliable flow velocities obtained using the HS and the LK methods are shown in Figures 34,35,36 and 37. The pattern of flow fields obtained with the two methods looks nearly identical. The magnitude of the flow obtained by using the HS method is almost same as the velocities obtained by using the LK method. The flow velocities near the sediment water interface are not calculated because the confidence measure in this region is close to zero as seen in Figures 34,35,36 and 37. The magnitude of the flow in the sediment ranges from 10^{-6} cm/s to 10^{-4}cm/s. The flow velocities obtained using the edge-tracking method are shown in Figures (38, 39, 40 and 41). The directions of the velocities are preserved in the edge tracking method, with typical velocities of approximately $2*10^{-4}$ cm/s.

Experiment1: The reliable flow velocities obtained using the HS and the LK methods are Figures 42, 43, 44 and 45. The pattern of flow fields obtained with the two methods looks nearly identical. The magnitude of the flow obtained by using the HS method is almost the same as the velocities that obtained by using the LK method. The magnitude of the flow in the sediment ranges from 10^{-6} cm/s to 10^{-3}cm/s. The flow velocities obtained by using the edge-tracking method are show in Figures 46 and 47. The directions of the velocities are preserved in the edge tracking method, with typical velocities of approximately $2*10^{-4}$ cm/s.

Critical assessment

Flow direction. In the flow reconstruction based on the real experimental images, one can clearly see flow from the overlying water into the sediment and from the sediment to the overlying water. The pore water advection occurs because of the hydraulic activities of the lugworm. The activities of the lugworm result in pressure fluctuations around the hydrostatic base line Volkenborn et al. (2010). Increase in pressure results in oxygenation of the sediment surrounding the burrow and an emergence of water through the sediment surface. If there is a reduction in pressure (reverse pumping) then the inflow of overlying water is seen (Volkenborn et al. 2010).

Flow dynamics. Forward (tail-to-head) pumping induces characteristic low-magnitude pressure oscillations. *Arenicola* shows long periods of continuous pumping, only interrupted by short periods of inactivity related to defecation at the surface and the pumping rate is almost steady (Matsui et al. 2011, Volkenborn et al., 2010). The addition of hydraulic pulses to the continuous water pumping causes abrupt pressure drops at unchanged pumping rates.

Flow magnitude. In sediment, the range of velocities reported by Volkenborn, et al. (2010) is 0.5-1mm/min. The water ascends into the over-lying region with a velocity of 4mm/min. This compares well with, the flow velocities obtained here, which are on the order of 0.1 mm/min in the sediment and 1 mm/min near the sediment-water interface (for all real image data sets).

Experimental artifacts. Water is close to incompressible; hence the incompressibility condition used in Equation (8) is a good assumption. However, the natural conditions reflect a three-dimensional physical space, as opposed to 2D images. Our approach thus implies that flow into the plane, or the contribution of dw/dz to the incompressibility equation, is small compared to velocity variations in x and y directions. Because the ant farm is thin, flow into the plane should indeed be small. However, this has not been independently verified and highlights the potential for impact of wall effects in the observational data (Polerecky et al., 2006).

Conclusions

In this thesis, the applicability of optical flow techniques to quantify flow fields in aquatic sediment is demonstrated. The use of established algorithms such as Horn-Schunck or Lukas-Kanade is possible through an iterative approach that accounts for diffusive/dispersive transport. Edge tracking, HS and LK methods work well for the real and test image data sets. In order to obtain reliable estimates, the confidence measure cut-off is important for the space filling in the HS and LK methods, while edge tracking by its nature focuses on regions in which flow is identifiable.

REFERENCES

1. S Baker, D Scharstein, J P Lewis, S Roth, M J Black, and R Szeliski. "A Database and Evaluation Methodology for Optical Flow." *IEEE 11th International Conference on Computer Vision.* (2007): 1-8.
2. J L Barron, D J Fleet, and S S Beauchemin. "Performance of optical flow techniques." *International Journal of Computer Vision* 12, no. 1 (1994): 43-77.
3. S Changming. "fast optical flow using cross -correlation and shortest path techniques." *Digital Image Computing: Techniques and Applicaions*, (1999): 143-148.
4. I Cohen, and H Isabelle. "Optical Flow and Phase Portrait Methods for Environmental Satellite Image Sequences." *Computer Vision—ECCV'96*, edited by Springer-Verlag. Vol. 1065. Heidelberg: springer, (1996): 141-150
5. J Eriksson. "Quasi-Newton Methods for Nonlinear Least Squares Focusing on Curvatures." *BIT Numerical Mathematics* 39 (1999): 228-254.
6. B Galvin, B Mccane, K Novins, D Mason, and S Mills. "Recovering motion fields: An evaluation of eight optical flow algorithms." *British Machine Vision Conference.* (1998): 195-204.
7. C Harris, and M Stephens. "A combined corner and edge detector." *Alvey vision conference.* (1988): 147--151.
8. B K Horn, and G B Schunck. "*Determining optical flow."* Report, Artificial Intelligence, MIT, Cambridge: MIT, (1981).

9. H Tzung-chi, G Zhang, T Guerrero, G Starkschall, K Lin, and K Forster. "Semi-automated CT segmentation using optic flow and Fourier interpolation techniques." *Computer Methods and Programs in Biomedicine* 84, no. 2 (2006): 124-134.
10. S P Jong and H H Joon "Contour matching: a curvature-based approach." *Image and Vision Computing* 16, no. 3 (1998): 181-189.
11. K Zdenek, K Mikolajczyk, and J Matas. "Tracking-Learning-Detection." *IEEE Transaction on Pattern Analysis And Machine Intelligence* 6, no. 1 (2010): 1-14.
12. A V Knyazev and M E Argentati. "On proximity of Rayleigh quotients for different vectors and Ritz values generated by different trial subspaces." *Linear Algebra and its Applications* 415, no. 1 (2006): 82-95.
13. A V Knyazev, and K Neymeyr. "Gradient Flow Approach to Geometric Convergence Analysis of Preconditioned Eigensolvers." *SIAM Journal on Matrix Analysis and Applications* 31, no. 2 (2009): 621-328.
14. T Lin and J L Barron. "Image Reconstruction Error for Optical Flow." *In Vision Interface* (Scientific Publishing Co), 1994: 73-80.
15. B D Lucas and T Kanade. "An iterative image registration technique with an application to stereo vision." *7th Internation Joint Conference on Artificial Intelligence.* (1981).
16. M R Mohammad, J Kim, S Sawazaki, K Okazaki, and S Tamura. "A scaled multigrid optical flow algorithm based on the least RMS error between real and estimated second images." *pattern recognition* 32, no. 4 (1999): 657-670.
17. J Malik, R Dahiya and G Sainarayan. "Harris Operator Corner Detection using Sliding Window Method." *International Journal of Computer Applications* 22, no. 1(2011): 28-37.

18. J Marcello, F Eugenio, and F Marques. "Methodology for the estimation of ocean surface currents using region matching and differential algorithms." *IEEE International Geoscience and Remote Sensing Symposium.* (2007): 882-885.
19. I Markovsky and S Van Huffel. "Overview of total least squares methods." *Signal Processing* 87, no. 10 (2007): 2283–2302.
20. G Y Matsui et al. "Mechanical imitation of bidirectional bioadvection in aquatic sediments." *Limnology and Oceanography: Methods (American Society of Limnology and Oceanography,)*, (2011): 84-96.
21. B McCane, K Novins, D Crannitch, and B Galvin. "On benchmarking optical flow." *Computer Vision and Image Understanding* 84, no. 1 (2001): 126-143.
22. J Filip J.R Meysman, O S Galaktionov, and J J Middelburg. "Irrigation patterns in permeable sediments induced by burrow ventilation: a case study of Arenicola marina." *Marine Ecology Progress Series* 303 (2005): 195-212.
23. A Mitchie, Y F Wang, and J K Aggarwal. "Experiments in computing optical flow with the gradient-based, multiconstraint method." *Pattern Recognition* 20, no. 2 (1987): 173-179.
24. A Osa, L Zhang, and M Hidetoshi. "Error sources and error reduction in gradient based method with local optimization." *IAPR Workshop on Machine Vision Applications.* Chiba, (1998). 8-22.
25. L Polereky, N Volkenborn, and P Stief. "High temporal resolution oxygen imaging in bioirrigated sediments." *Environ.Sci.Technology* 40 (2006): 5763-5769.
26. G M Quenot, J Pakleza, and T Kowalewski. "Particle image velocimetry with optical flow." *Experiment In Fluids* 25, no. 3 (1998): 177-189.

27. K S Rhode, T Lambrou, D J Hawkes, and A M Seifalian. "Novel approaches to the measurement of arterial blood flow from dynamic digital X-ray images." *IEEE Transactions on Medical Imaging* 4 (2000): 50-513.
28. A E Scheidegger. “General theory of dispersion in porous media.” *Journal of Geophysical Research*, (1961): 3273-3278.
29. D H Shull, J M Benoit, C Wojocik, and J R Senning. "Infaunal burrow ventilation and pore-water transport in muddy sediments." *Estuarine, Coastal and Shelf Science* 83, no. 3 (2009): 277-286.
30. S M Song, and R M Leahy. "Computation of 3-D velocity fields from 3D cine CT images of a human heart." *IEEE Transactions on Medical Imaging* 10, no. 3 (1991): 295-306.
31. C Tomasi, and T Kanade. "Detection and Tracking of Point Features." *International Journal of Computer Vision* 9 (1991): 137--154.
32. N Volkenborn, L Polerecky, D S Wethey, and S A Woodin. "Oscillatory porewater bioadvection in marine sediments induced by hydraulic activities of Arenicola marina." *Limnology and Oceanography* 55, no. 3 (2010): 1231-1247.
33. N Volkenborn, L Polerecky, S.I.C Hedtkamp, J V Beusekom, and D Beer. "Bioturbation and bioirrigation extend the open exchange regions in permeable sediments." *Limnology and oceanography (American Society of Limnology and Oceanography)* 52, no. 5 (2007): 1898-1909.
34. J Weber, and J Malik. "Robust computation of optical-flow in a multiscale differential framework." *International Journal of Computer Vision* 14, no. 1 (1995): 67-81.
35. A Yilmaz, J Omar, and M Shah. "Object tracking: A survey." *ACM Computing Survey* 38, no. 4 (2006): 1-45.

36. D Ziou, and T Salavtore. "Edge Detection Techniques - An Overview." *International Journal of Pattern Recognition and Image Analysis* 8 (1998): 537-559.

Figures

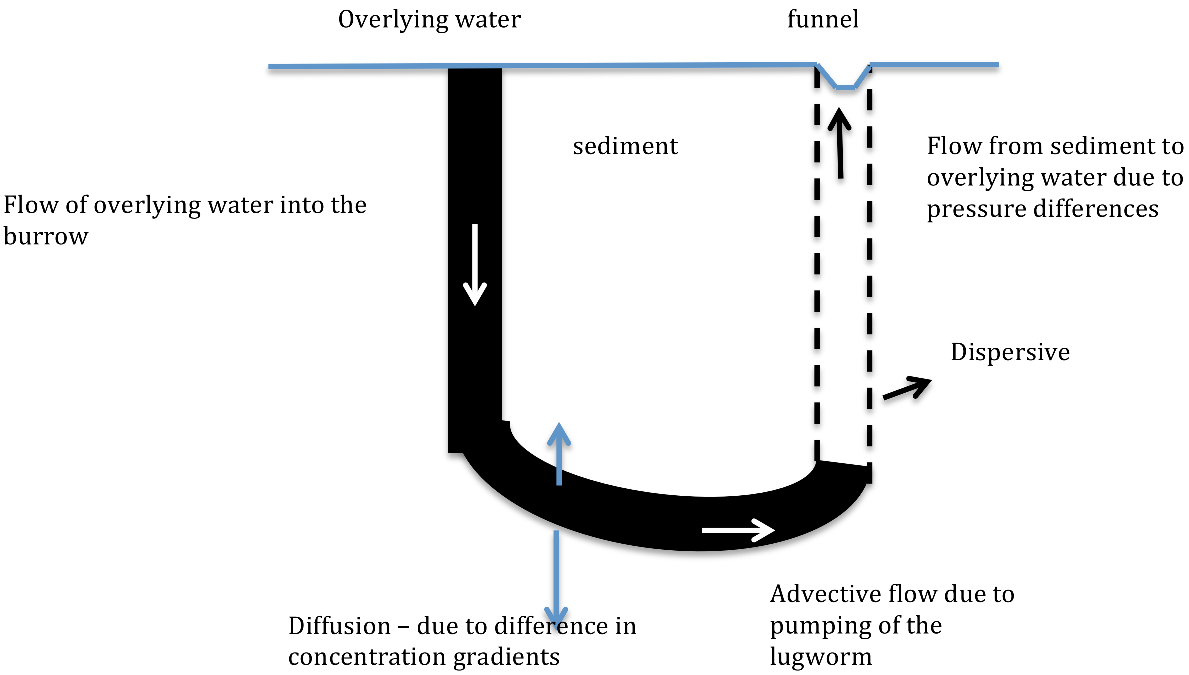

Figure 1: flow of water in sediment due to Lugworm after (Meysman, Galaktionov and Middelburg 2005) The diffusive transport is shown by blue arrows, advective flow is shown by white arrow and dispersive transport is shown by black arrow

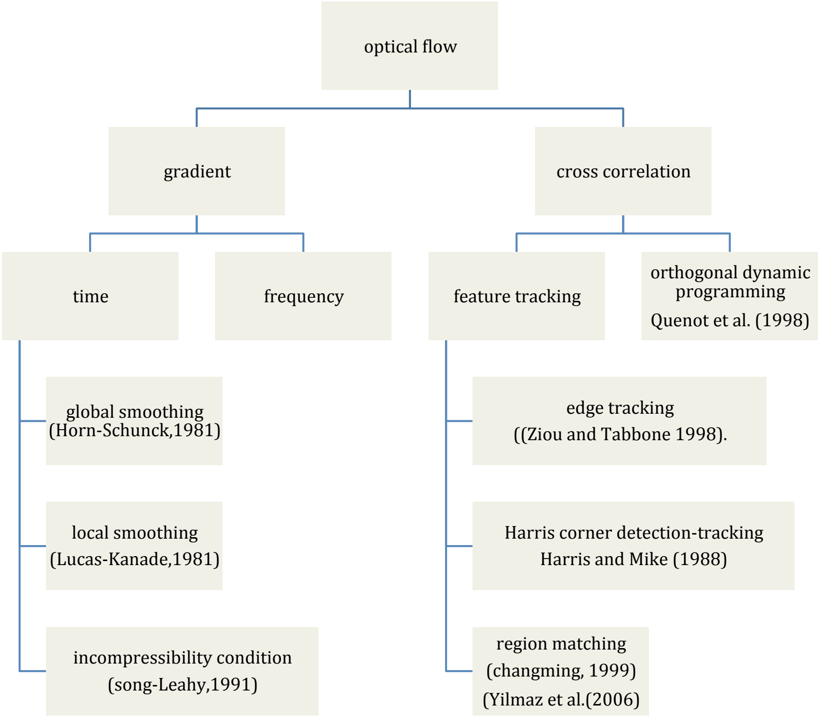

Figure 2: grouping for different methods of determining optical flow

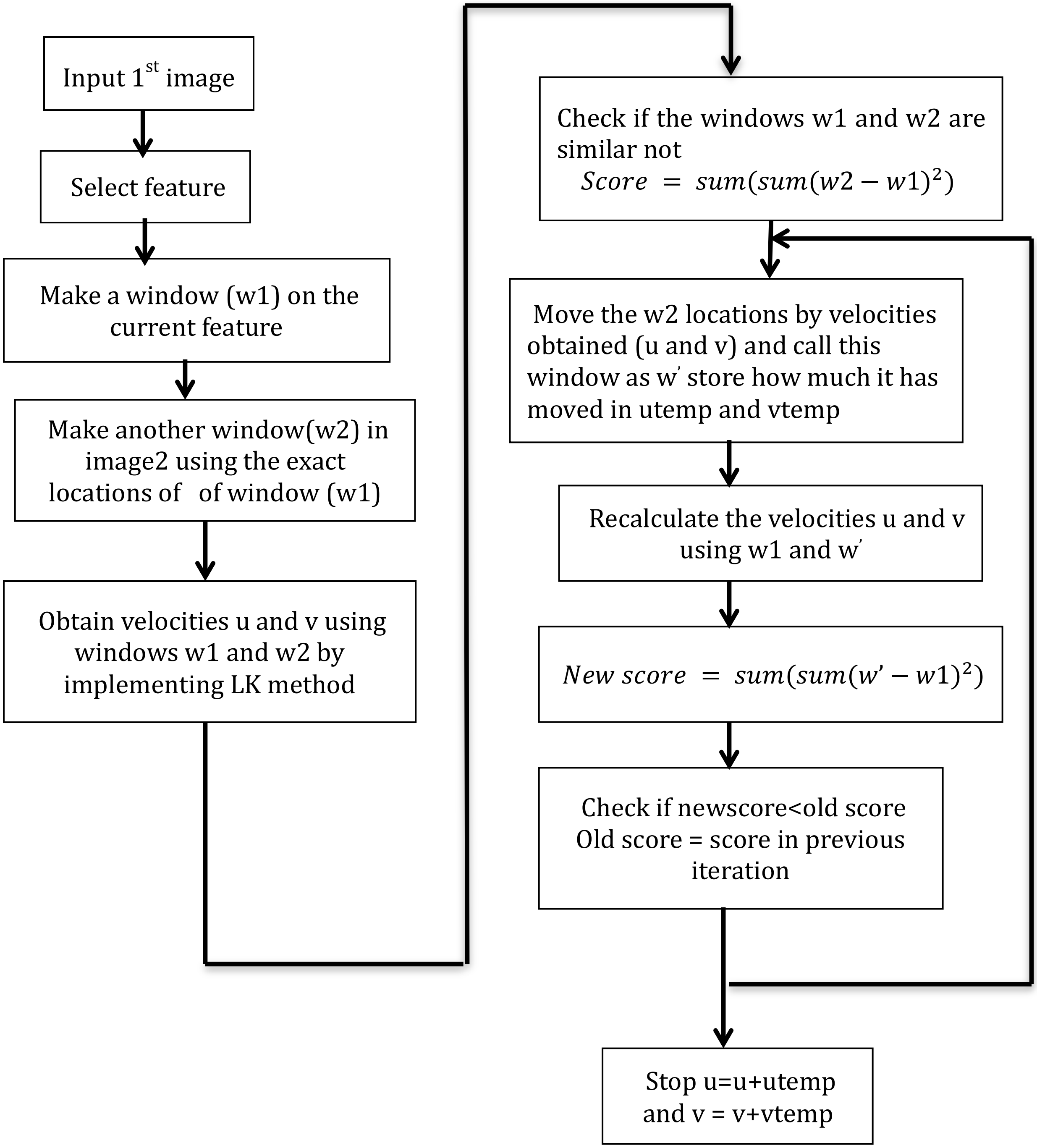

Figure 3: flow chart for tracking technique

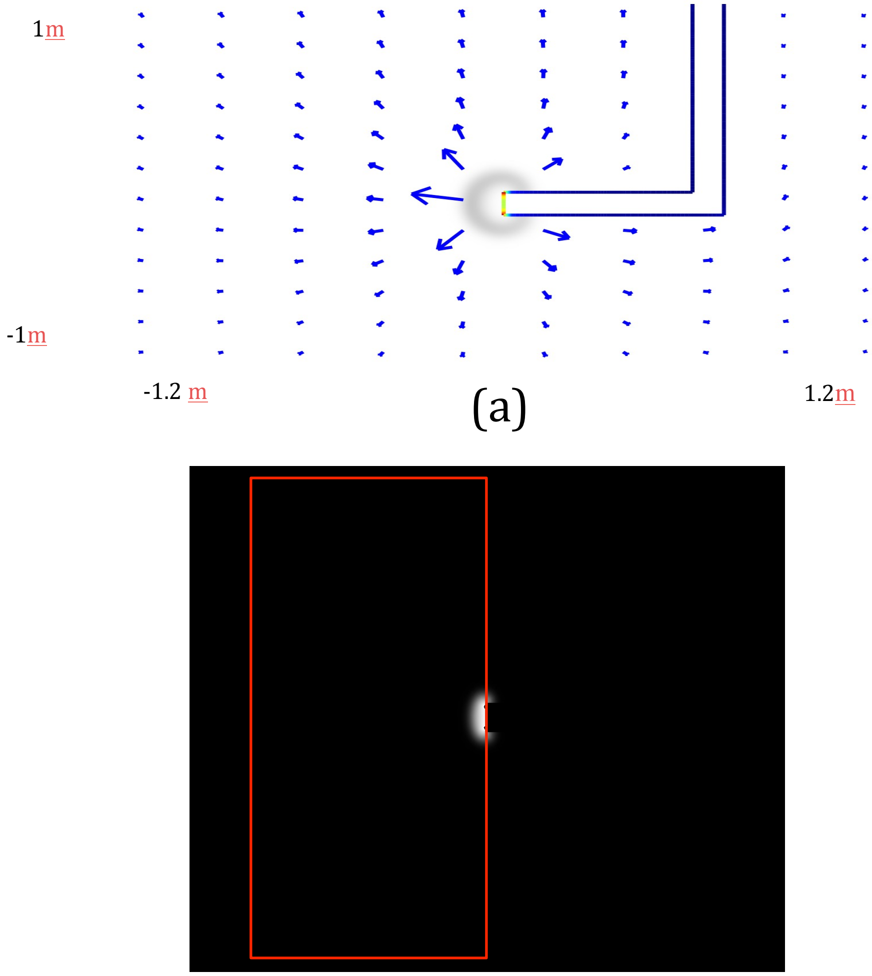

(a)

(b)

Figure 4 (a) mimics the antfarm setup. The gray region represents the tracer and the arrows represent the direction in which the tracer has moved over time. (b). The white region represents the presence of tracer and the black region represents the sediment. The exported images are of the size 1000X1333. However, to analyze the images the burrow is cropped out. The size of images that are analyzed with different optical flow methods is 1000X687.

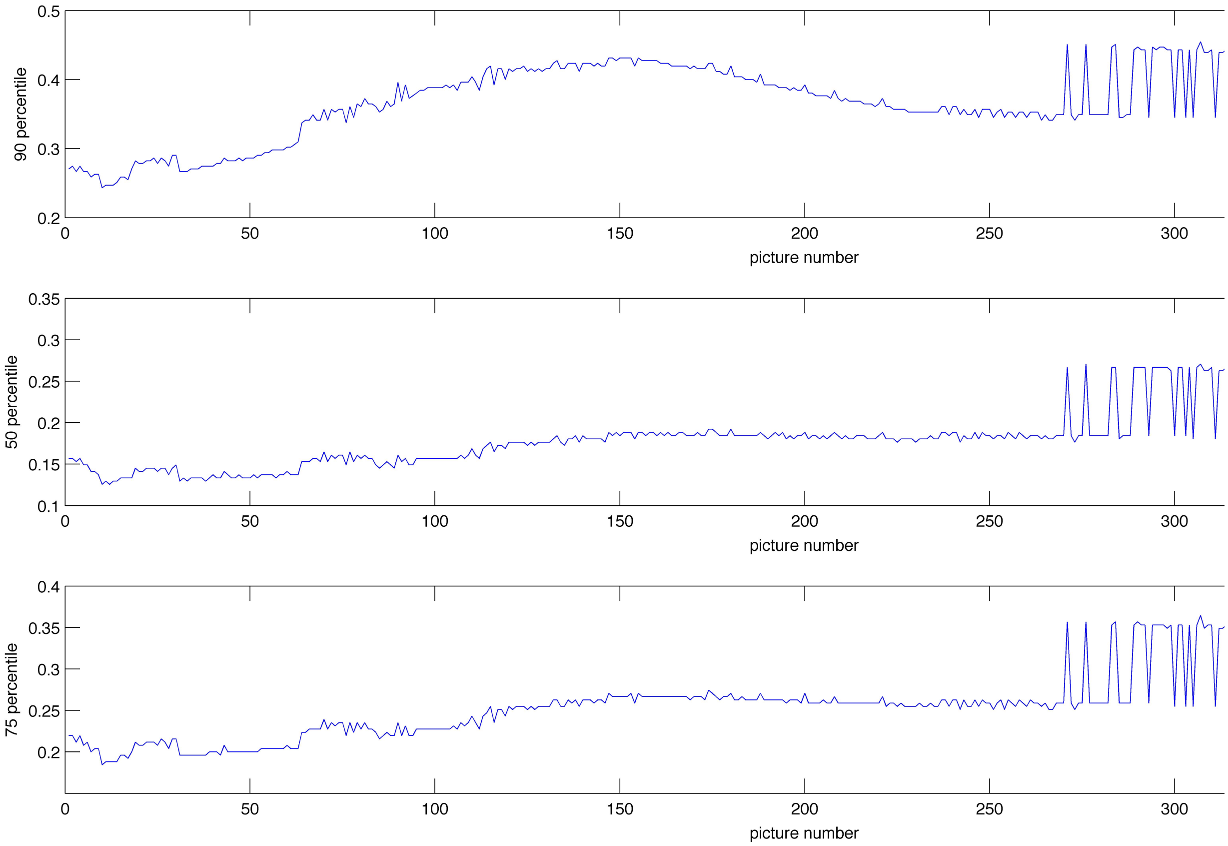

Figure 5 a, b and c represents the 50,90 and 75 percentile intensity (I) per image on Y-axis and image number on X-axis.

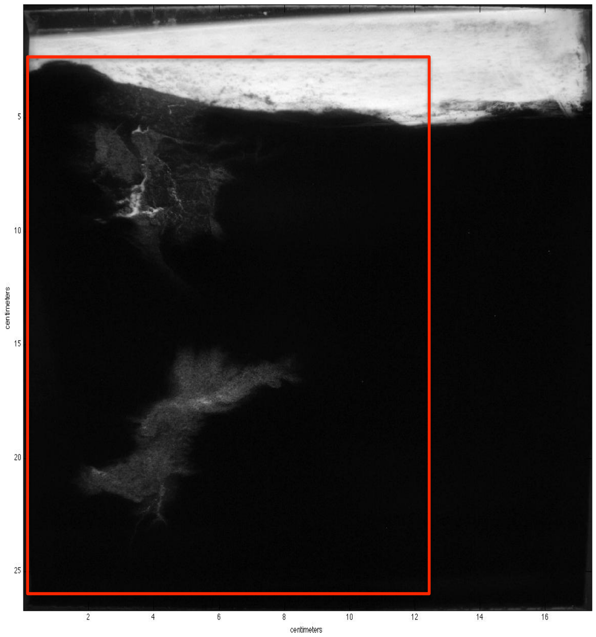

Figure 6 The image of fluorescent flow tracer in the acrylic ant farm style aquarium measuring 22cm x 44.5cm x 2.2cm taken on oct26th. The aquarium consists of sediment containing *Abarenicola pacifica*. The aquarium was maintained in the dark. Then, fluorescein was added and its distribution in the sediment – caused by pumping of the arenicolid worm. The red box represents the region of interest in which optical flow is calculated.

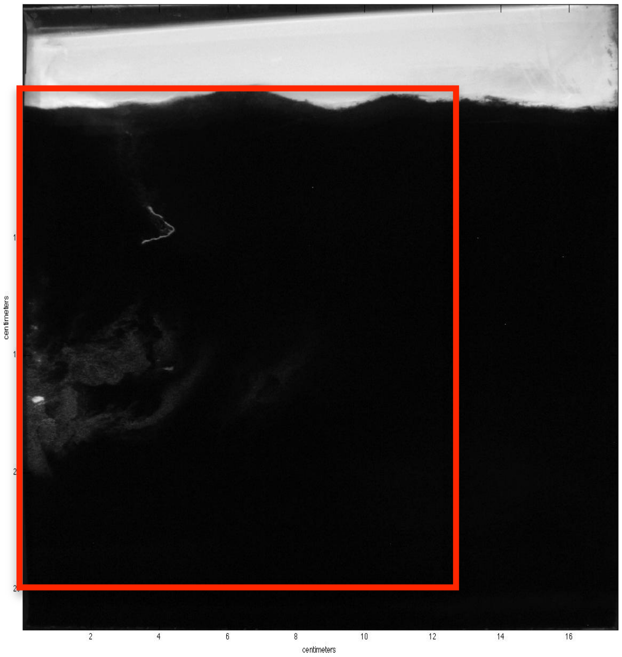

Figure 7 As Figure 6, but for Nov 2

Figure 8 As Figure 6 but for June 28

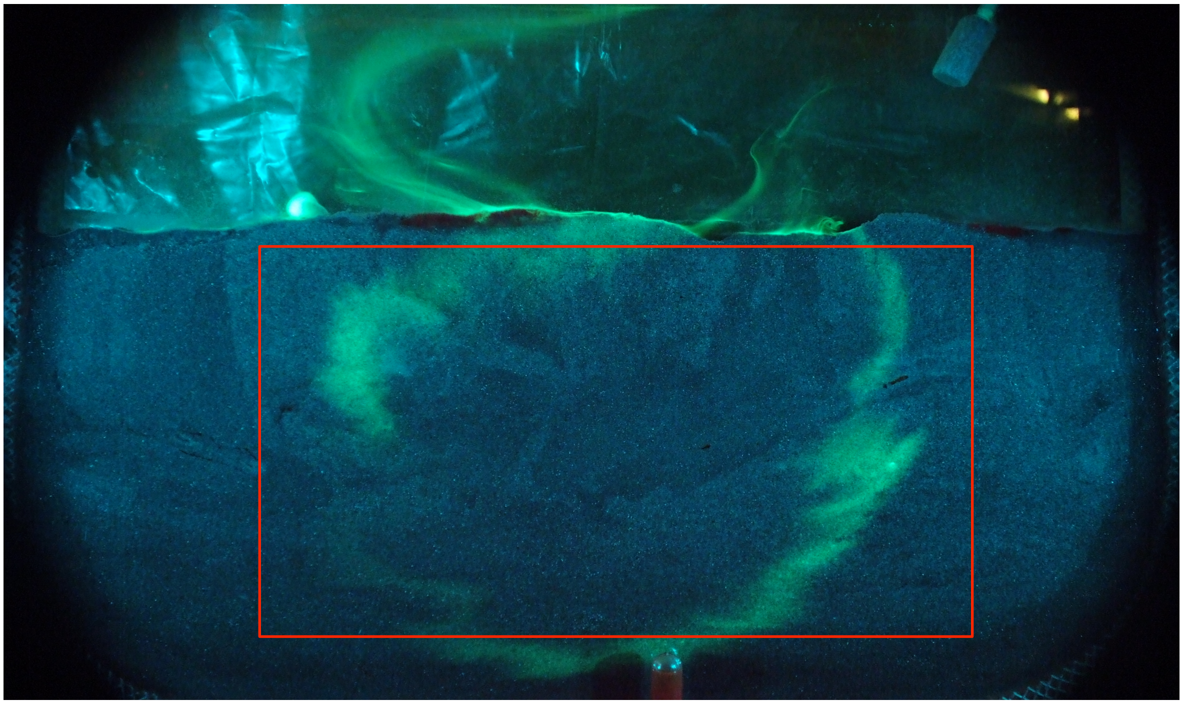

Figure 9 : As Figure 6 but for November 2009

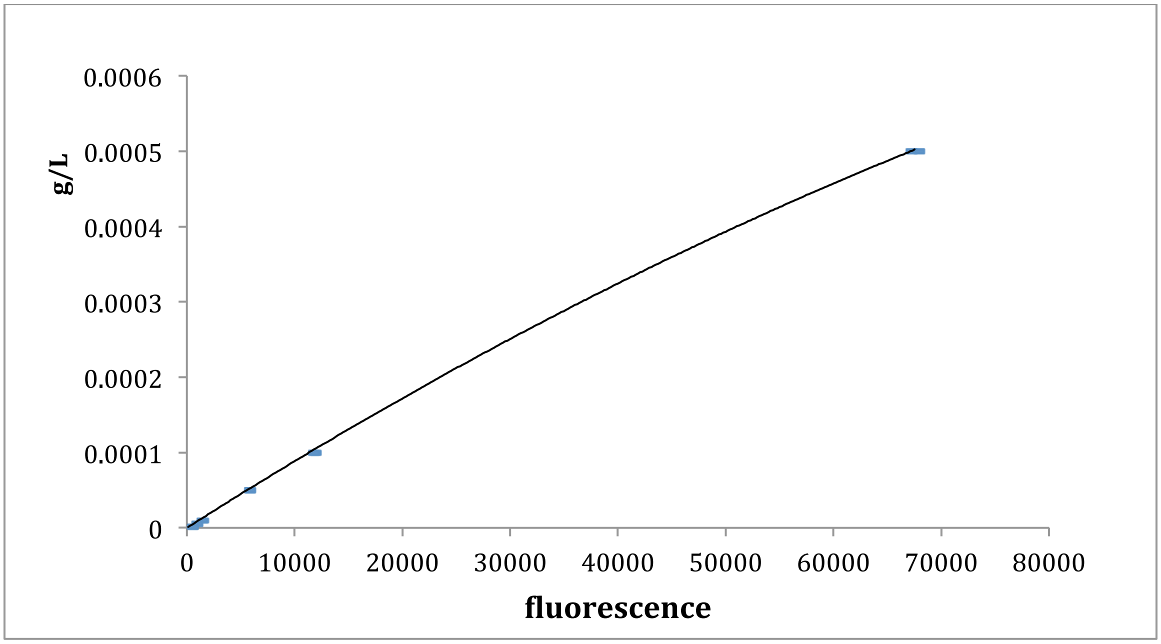

Figure 10 The calibration curve - fluorescein concentration on Y-axis and intensity on X-axis. The curve concentration (C) and intensity (I) varies linearly.

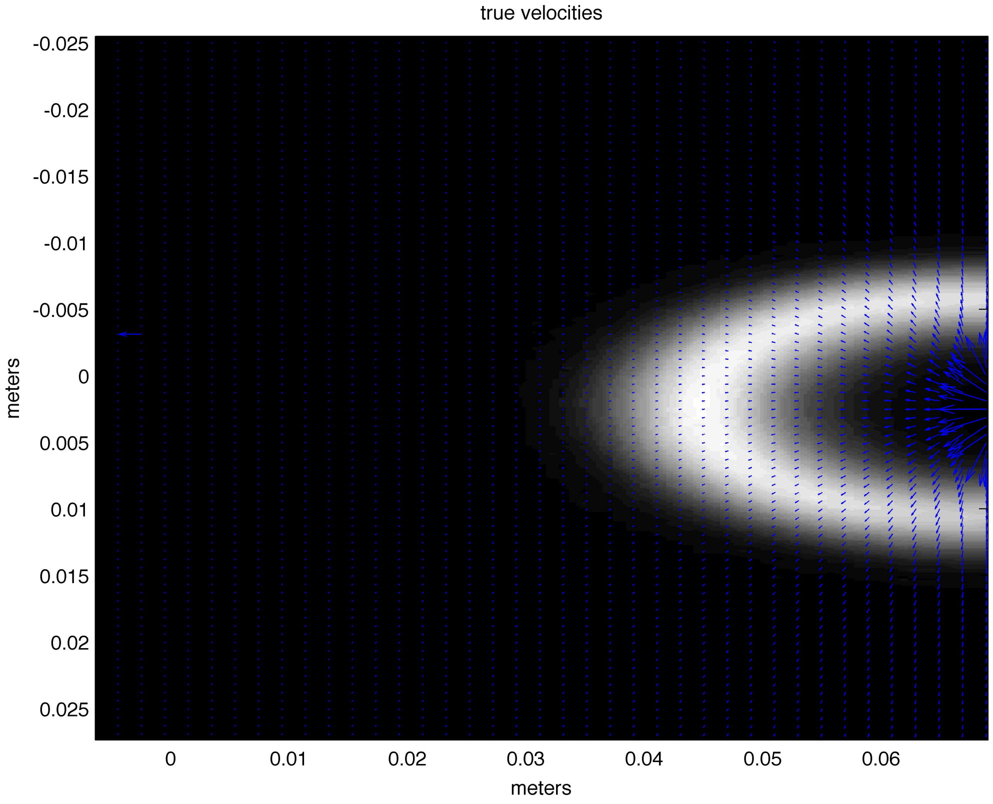

Figure 11 velocities and tracer distribution obtained from reactive transport simulation with a known flow field

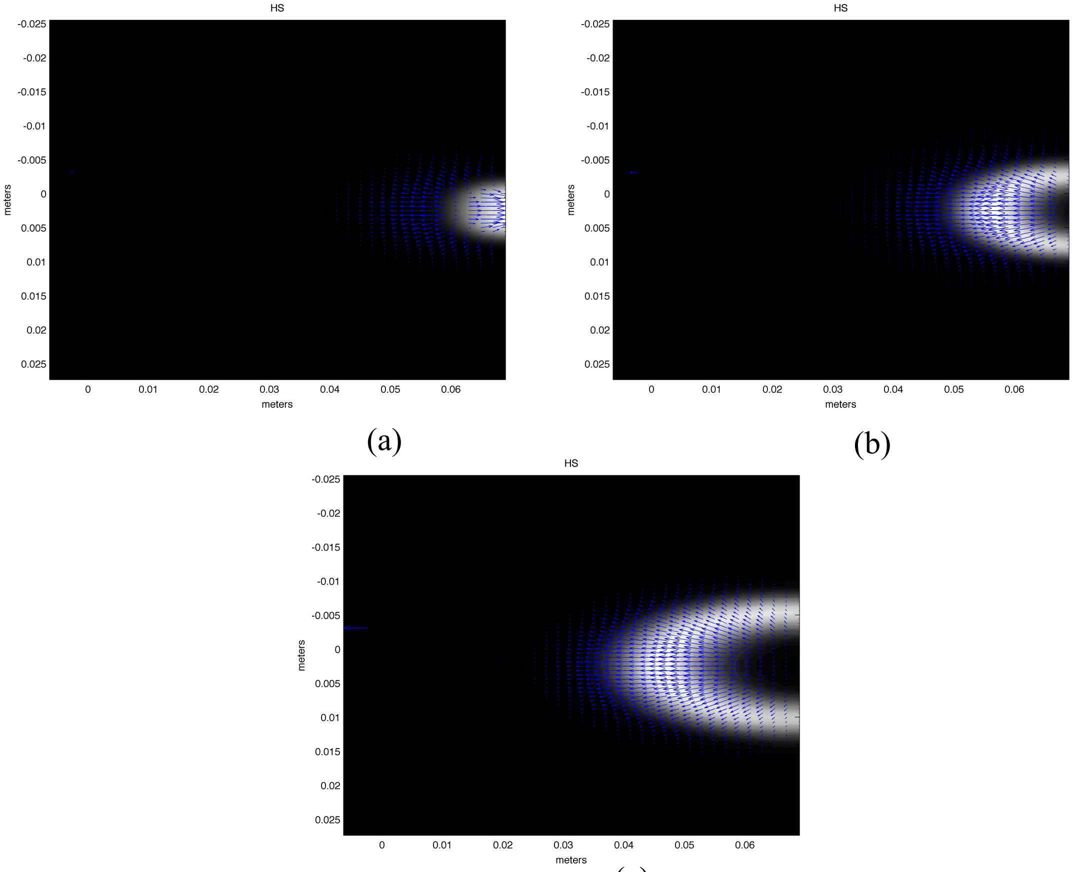

(a) (b)

(c)

Figure 12 The velocities obtained from the Horn Schunck method are plotted on the images taken at (a) 10 seconds, (b) 30 seconds and (c) 80 seconds. The reference arrow at (0.01,0) is of the magnitude 10^{-4}m/s.

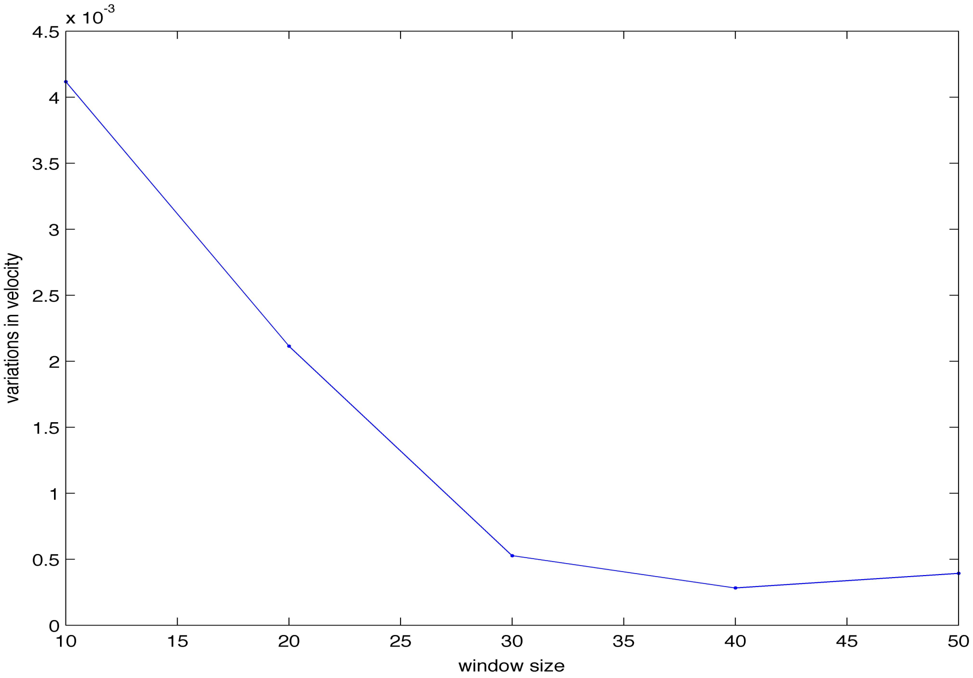

Figure 13 The graph is plotted with variation velocity at different window sizes on Y-axis and window sizes on X-axis. The above graph is drawn by using the velocities obtained from LK method on images taken at 30-40seconds

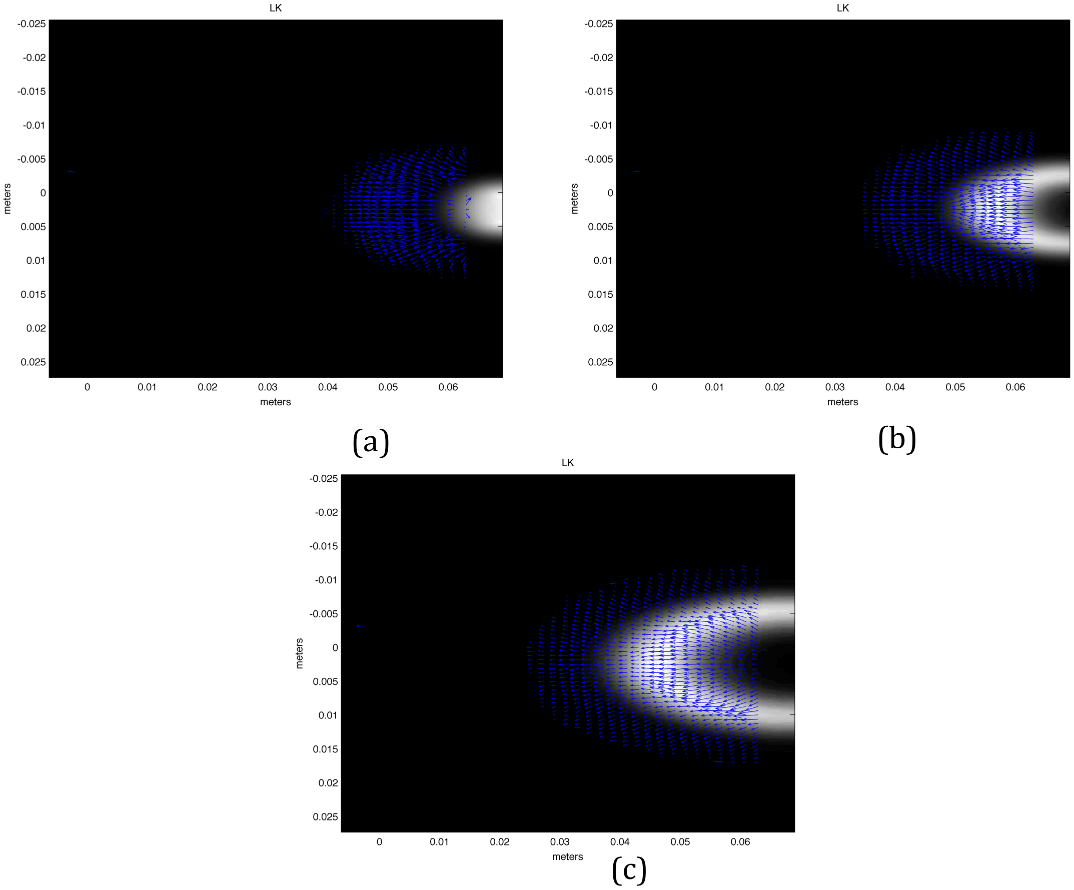

(a) (b) (c)

Figure 14 The velocities obtained from the LK method are plotted on the images taken at (a) 10 seconds, (b) 30 seconds and (c) 80 seconds. The reference arrow at (0.01,0) is of the magnitude 10^{-4}m/s.

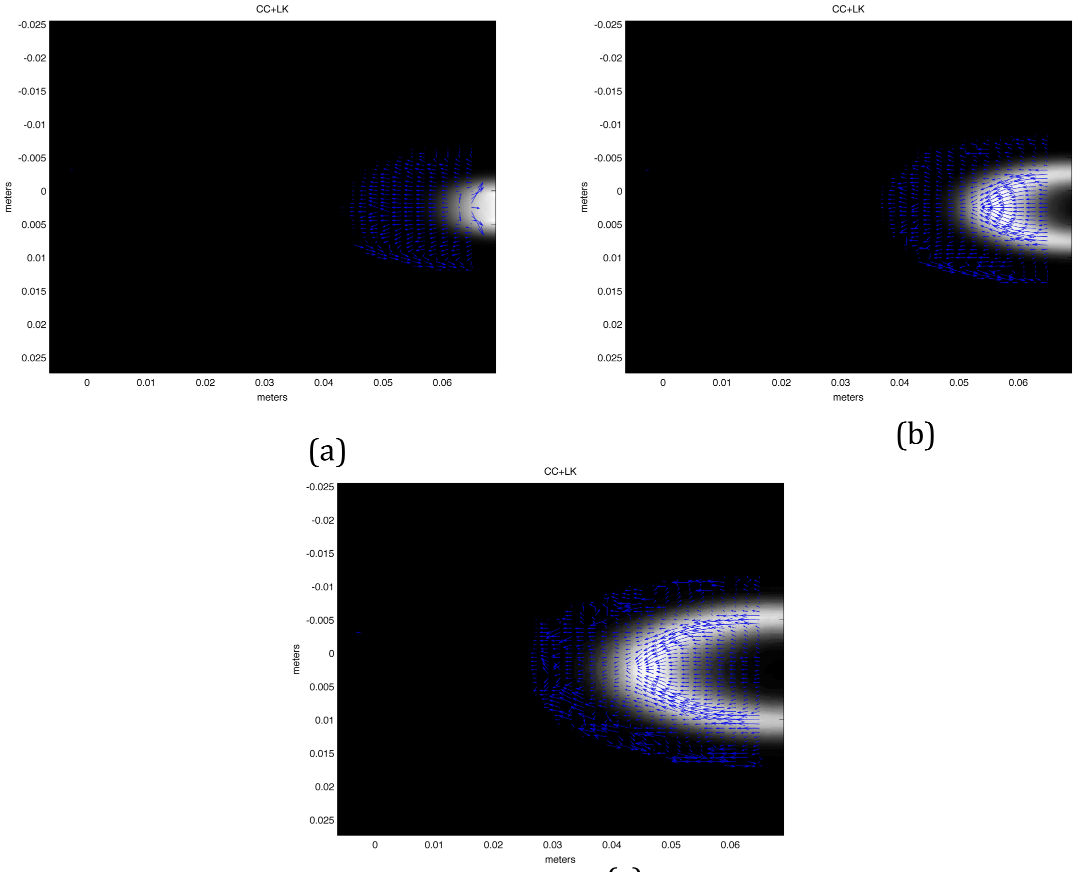

(a)

(b)

(c)

Figure 15 The velocities obtained from the CC+LK method are plotted on the images taken at (a) 10 seconds, (b) 30 seconds and (c) 80 seconds. The reference arrow at (0.01,0) is of the magnitude 10^{-4}m/s.

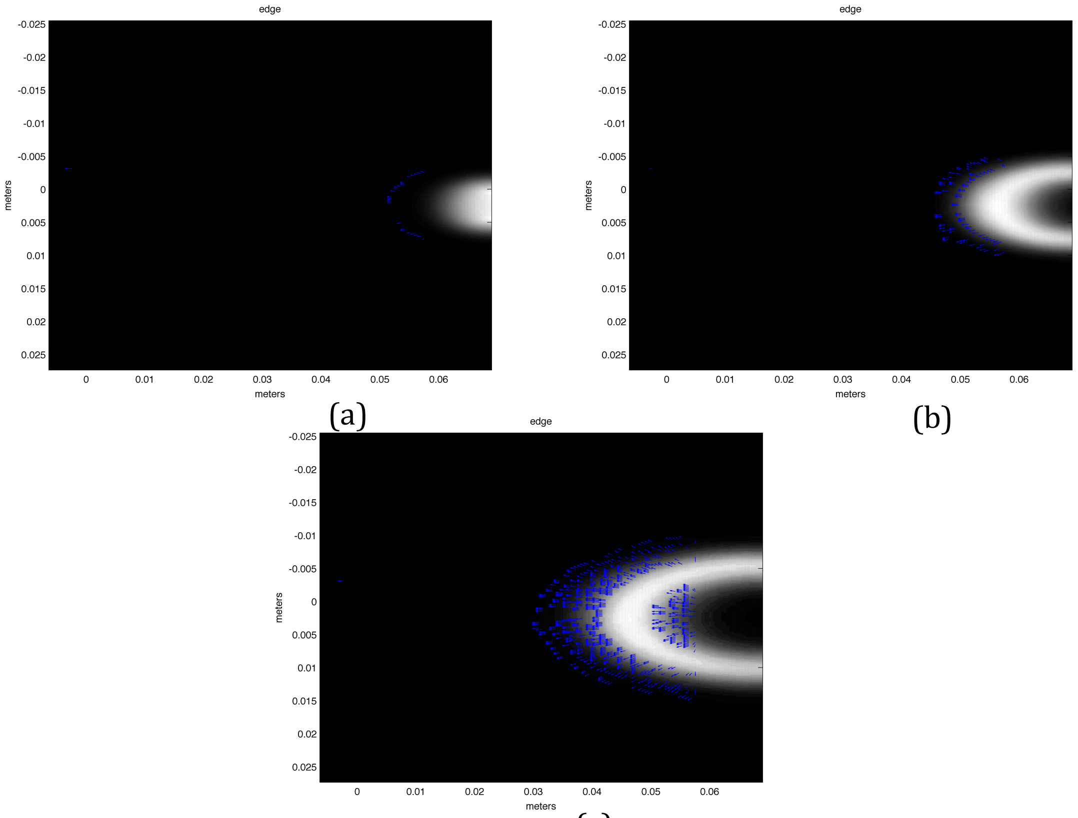

(a)

(b)

(c)

Figure 16 The velocities obtained from the edge tracking method are plotted on the images taken at (a) 10 seconds, (b) 30 seconds and (c) 80 seconds. The reference arrow at (0.01,0) is of the magnitude 10^{-4}m/s.

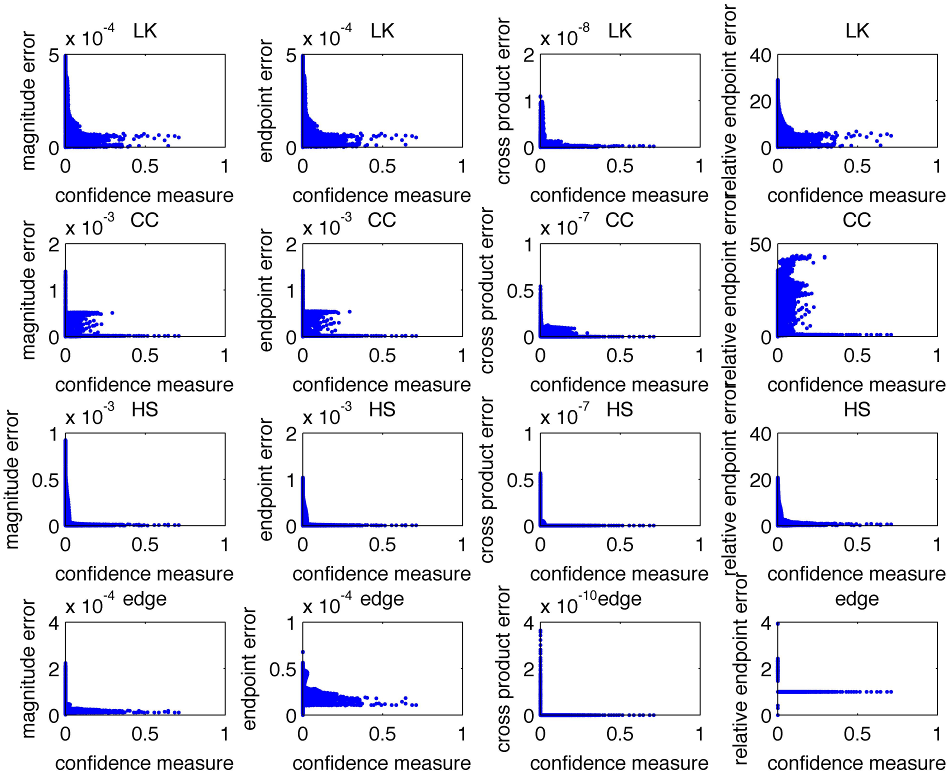

Figure 17 The confidence measure vs. magnitude, cross product, end point and relative endpoint error graphs are plotted for the images taken at 10 seconds.

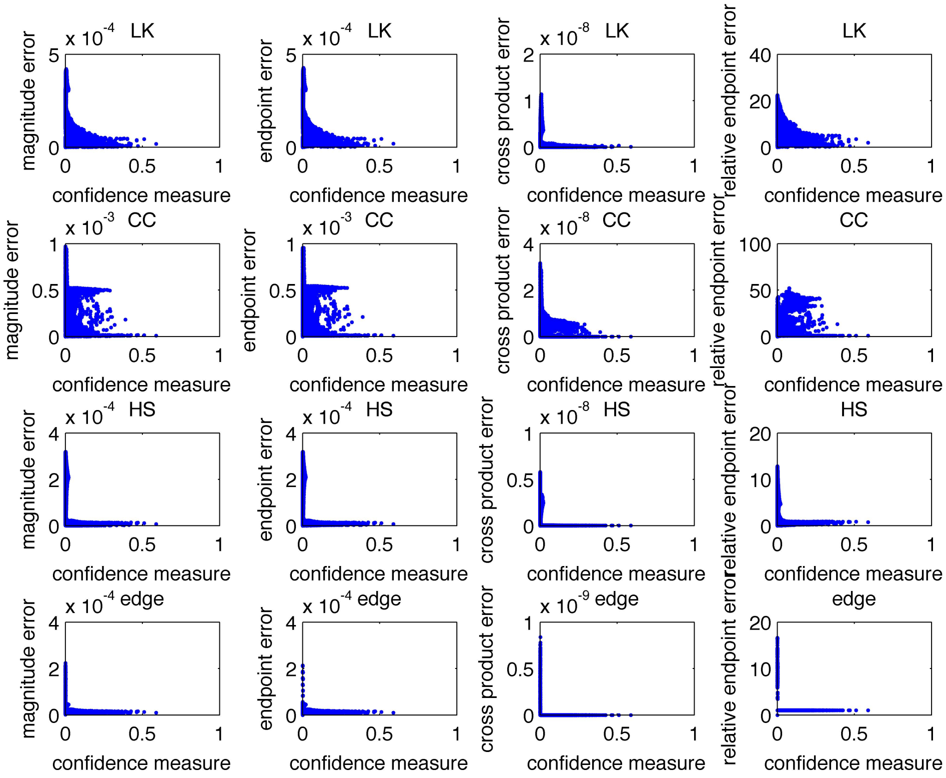

Figure 18 The confidence measure vs. magnitude, cross product, end point and relative endpoint error graphs are plotted for the images taken at 30 seconds.

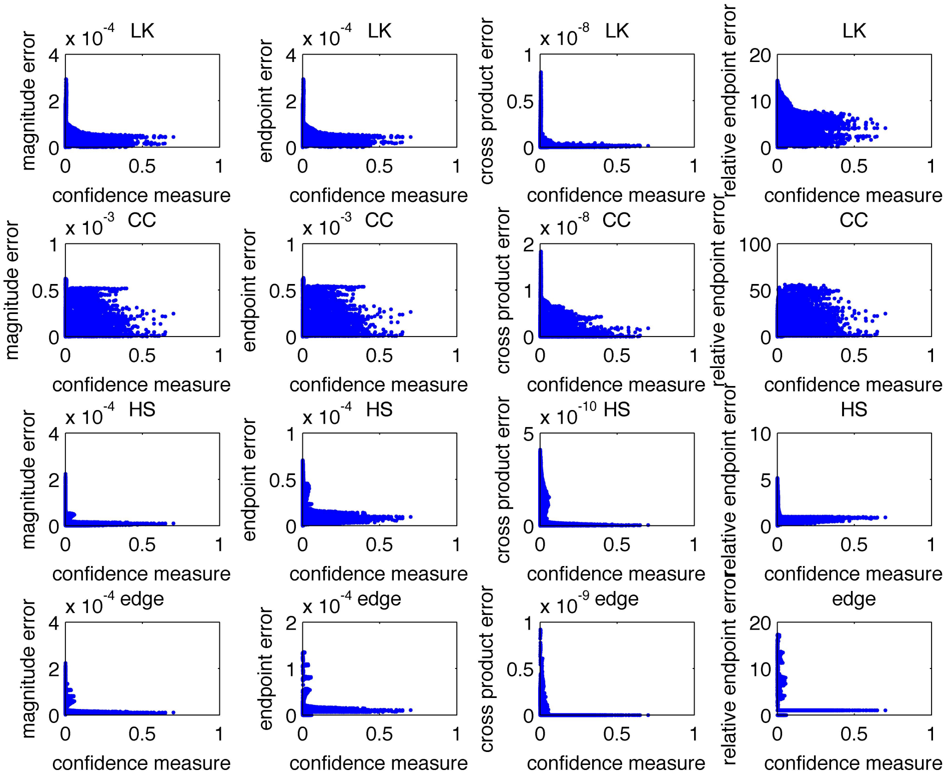

Figure 19 The confidence measure vs. magnitude, cross product, end point and relative endpoint error graphs are plotted for the images taken at 80 seconds.

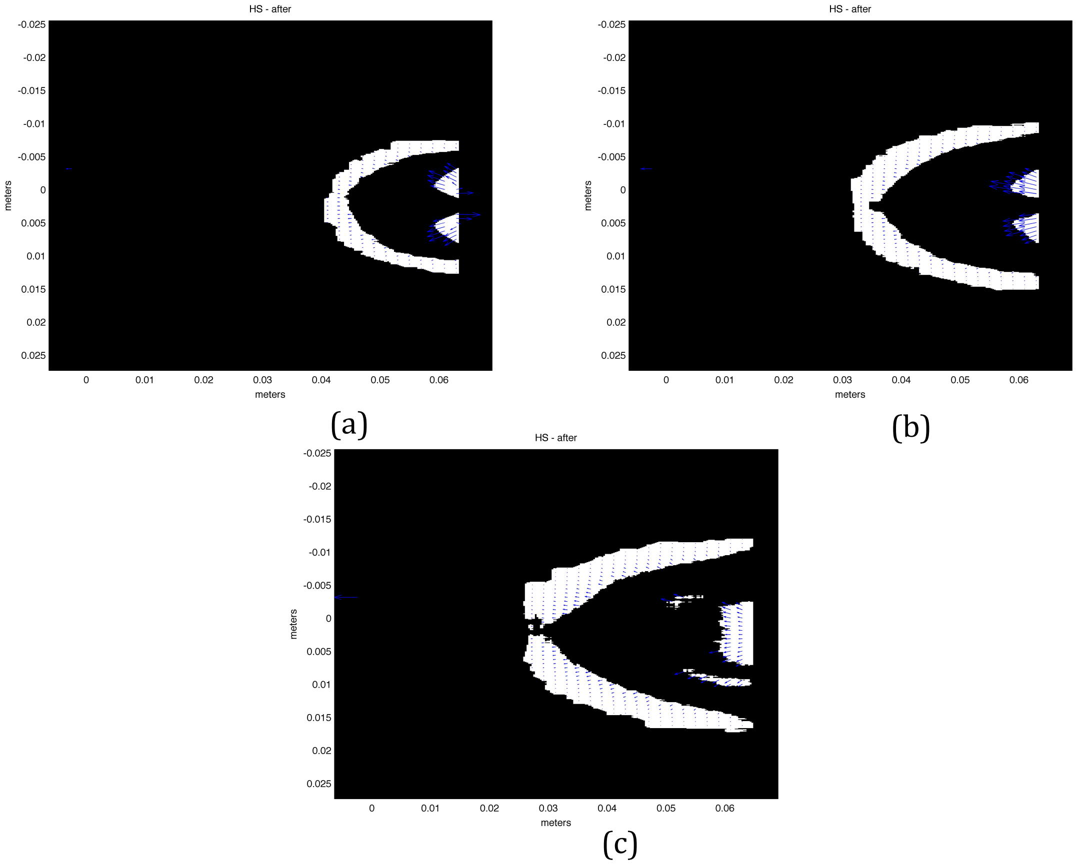

Figure 20 The reliable velocities obtained from the Horn Schunck method are plotted on the regions of the images taken at (a) 10 seconds, (b) 30 seconds and (c) 80 seconds with a confidence measure greater than 0.005. The reference arrow at (0.01,0) is of the magnitude 10^{-4}m/s.

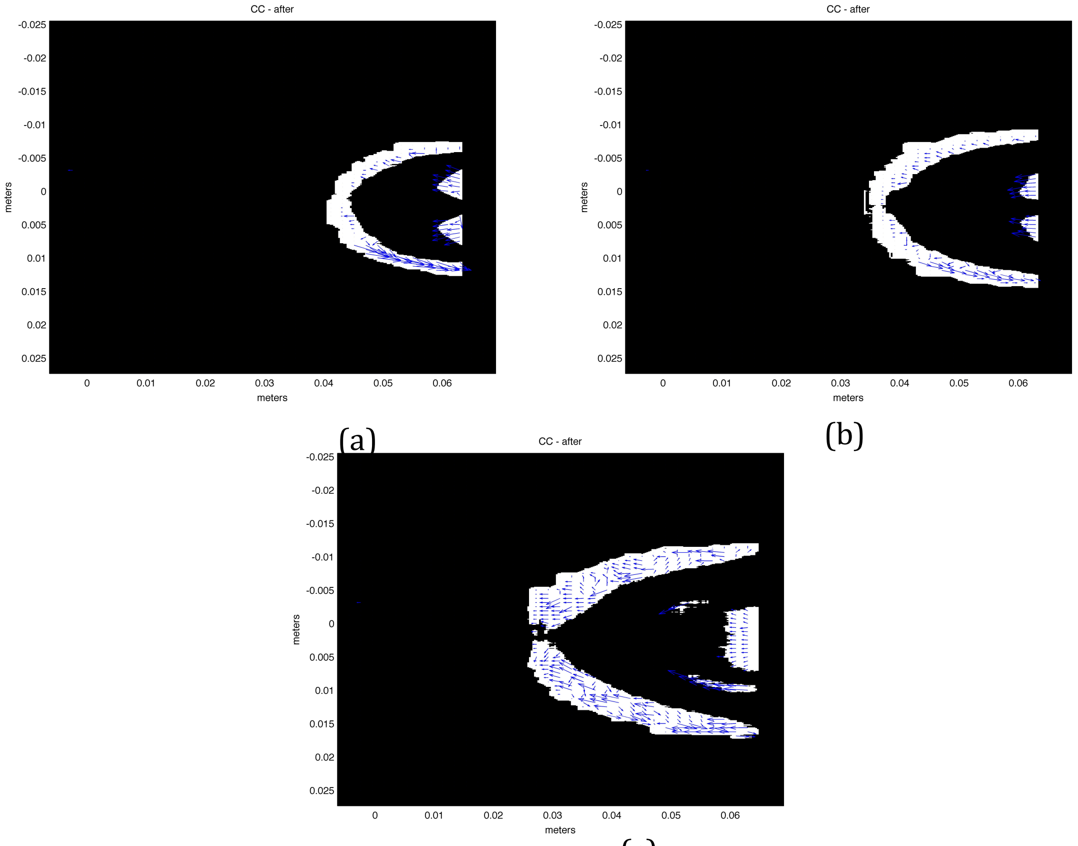

(a)

(b)

(c)

Figure 21 The reliable velocities obtained from the CC+LK method are plotted on the regions of the images taken at (a) 10 seconds, (b) 30 seconds and (c) 80 seconds with a confidence measure greater than 0.005. The reference arrow at (0.01,0) is of the magnitude 10^{-4}m/s.

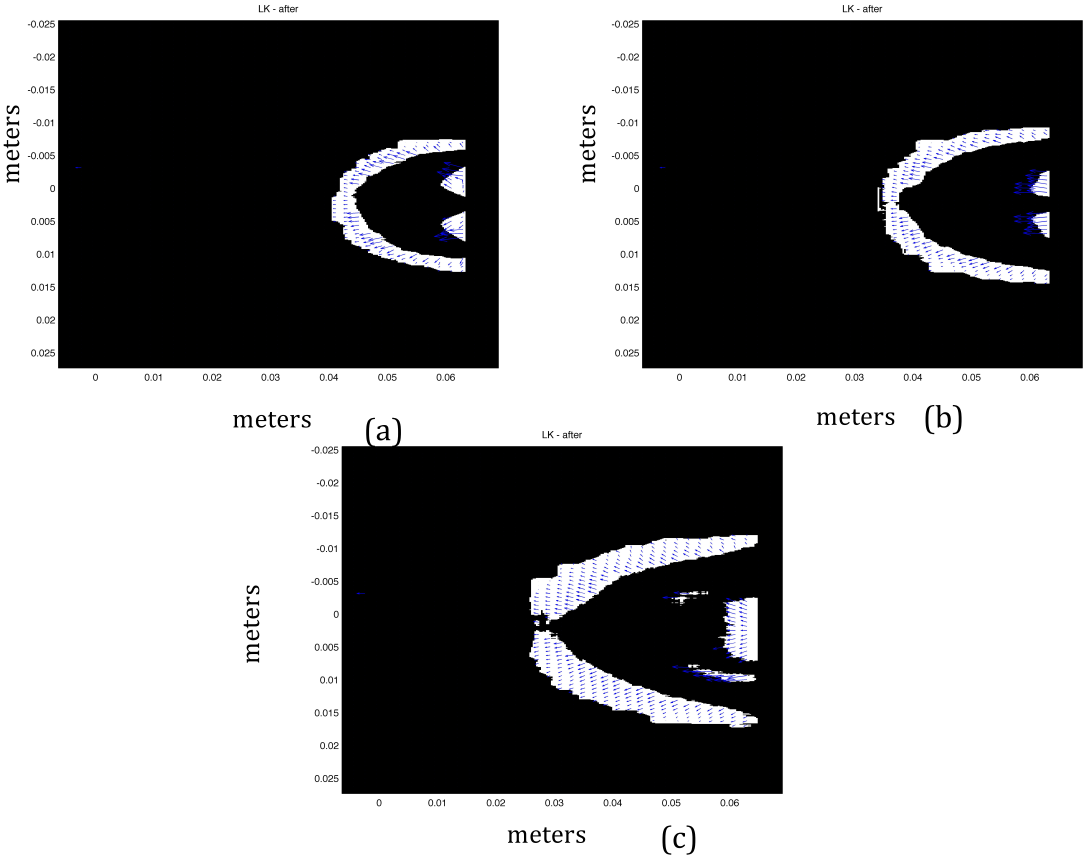

Figure 22 The reliable velocities obtained from the LK method are plotted on the regions of the images taken at (a) 10 seconds, (b) 30 seconds and (c) 80 seconds with a confidence measure greater than 0.005. The reference arrow at (0.01,0) is of the magnitude 10^{-4}m/s.

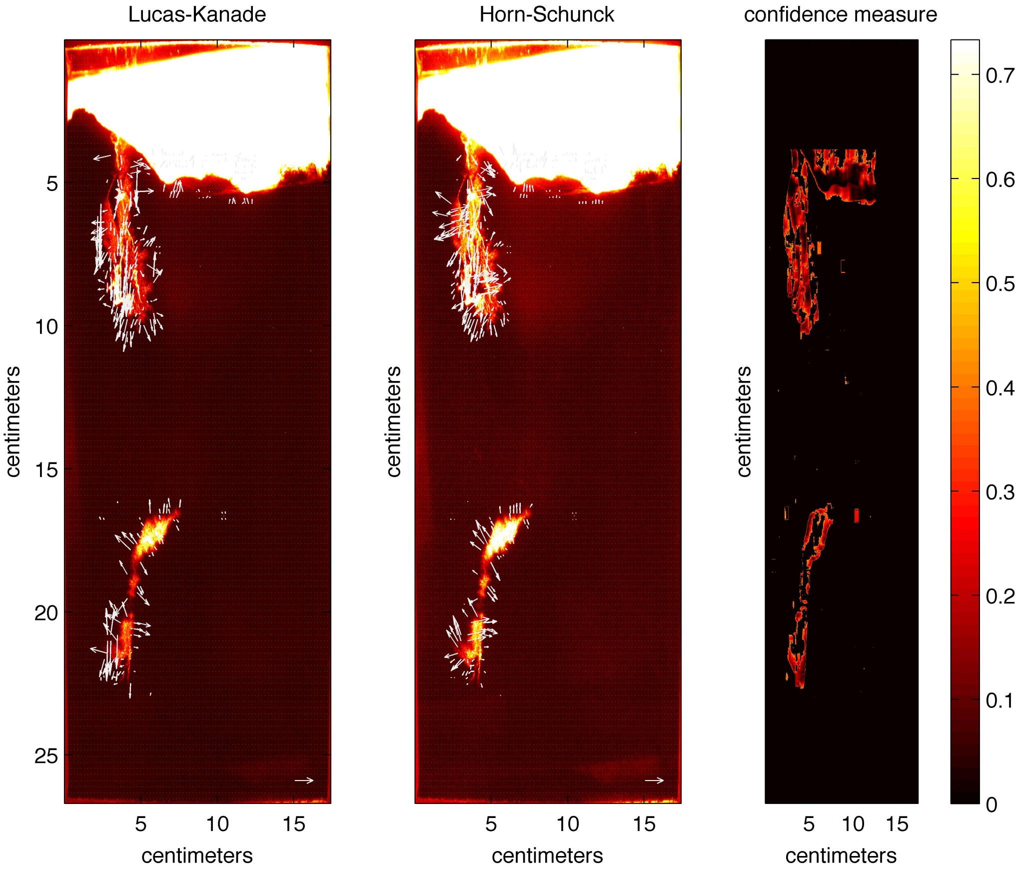

Figure 23 The optical flow velocities obtained using HS and LK methods are plotted on the images (real images taken on 26th October) used to calculate the optical flow. Bright color in the two left panels denote high tracer concentration, most evident in the overlying water. The confidence measure (right panel, with color bar) shows the region where we have actual information in warmer colors. The flow in the regions where the confidence measure is high is considered reliable. The arrow located at (15,26) is the reference arrow of length $1.8948*10^{-04}$m./s and $2.8479*10^{-04}$m/s for HS and LK methods respectively.

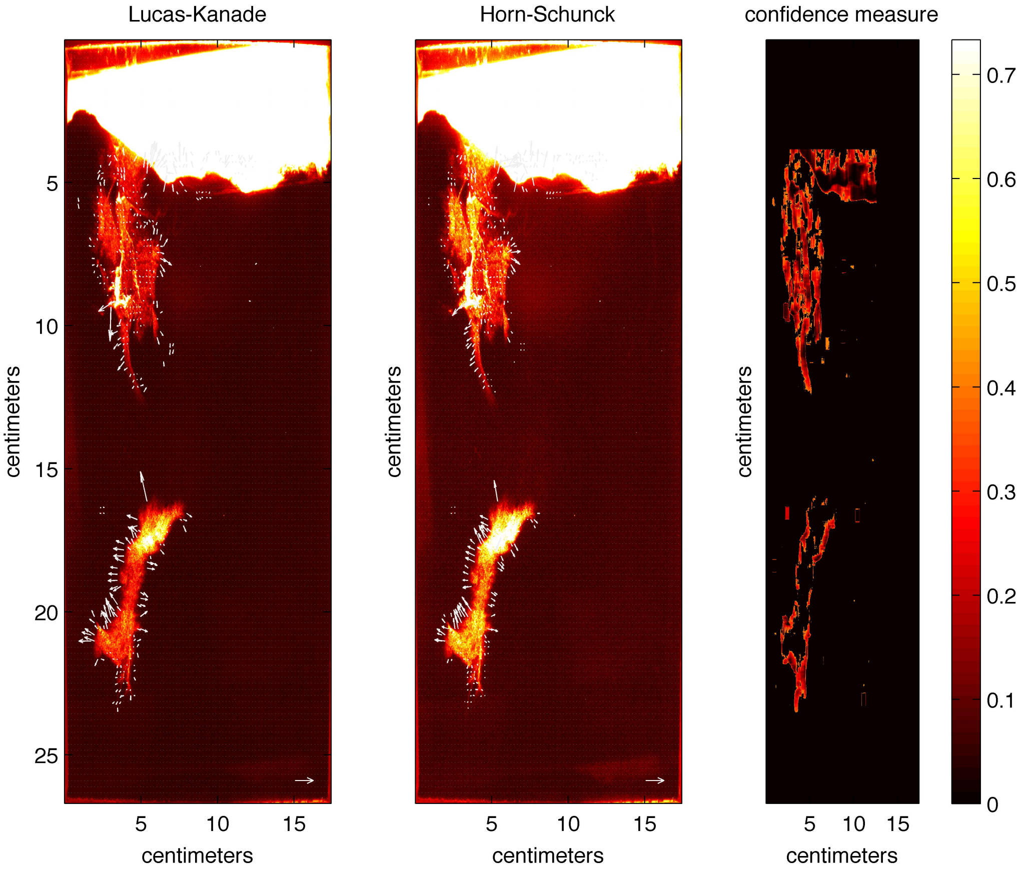

Figure 24 As Figure 20, but for a different timeslice.

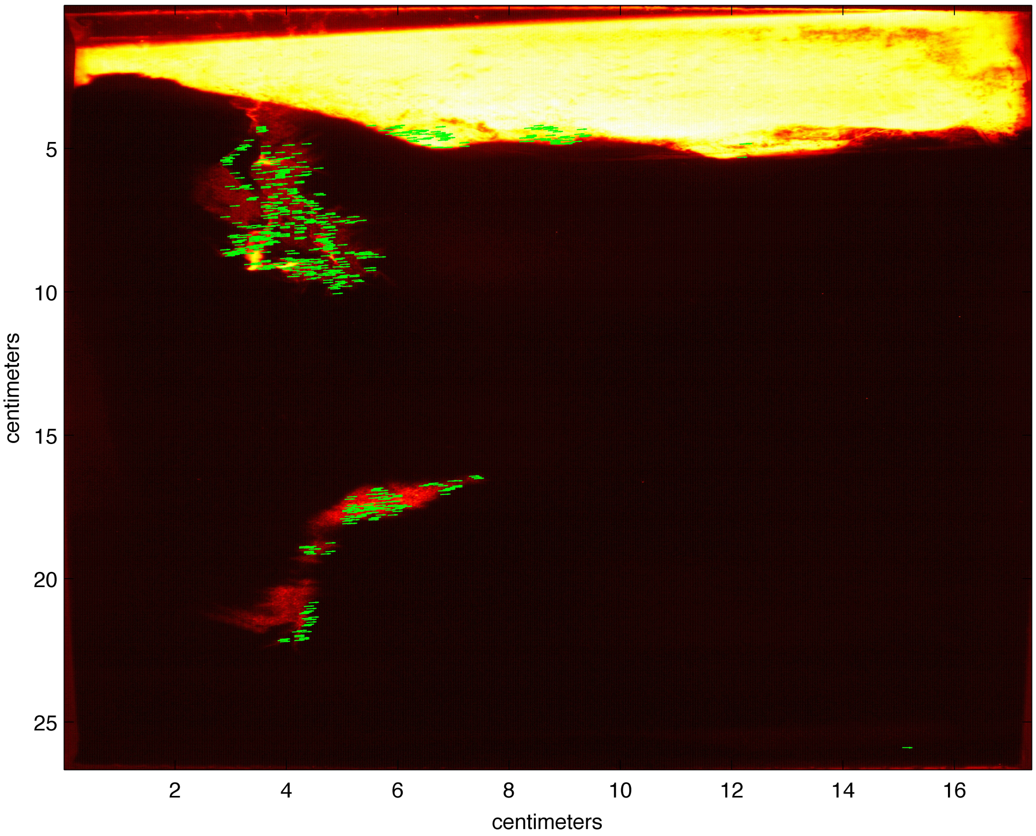

Figure 25 The optical flow velocities obtained using edge tracking methods are plotted on the images (real images taken on 26th October) used to calculate the optical flow. The reference arrow located at (15,26) is of length 1.8948*10^{-04}m/s

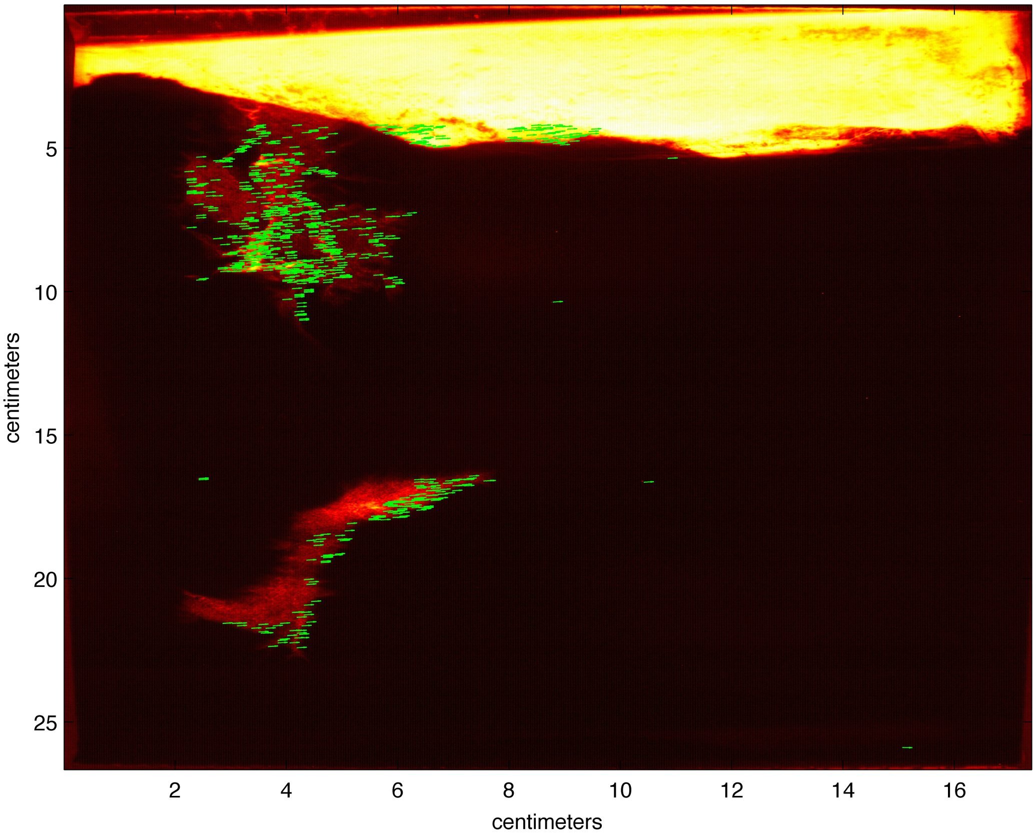

Figure 26 As Figure 22 but for a different timeslice.

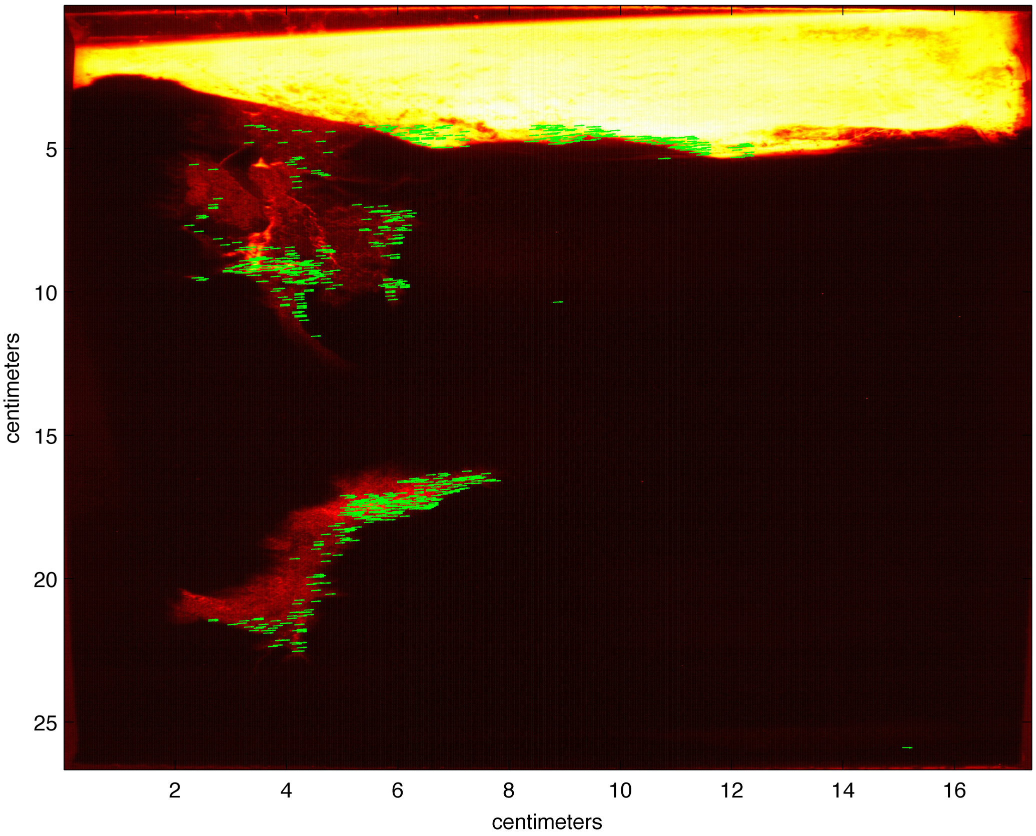

Figure 27 As Figure 22, but for a different timeslice.

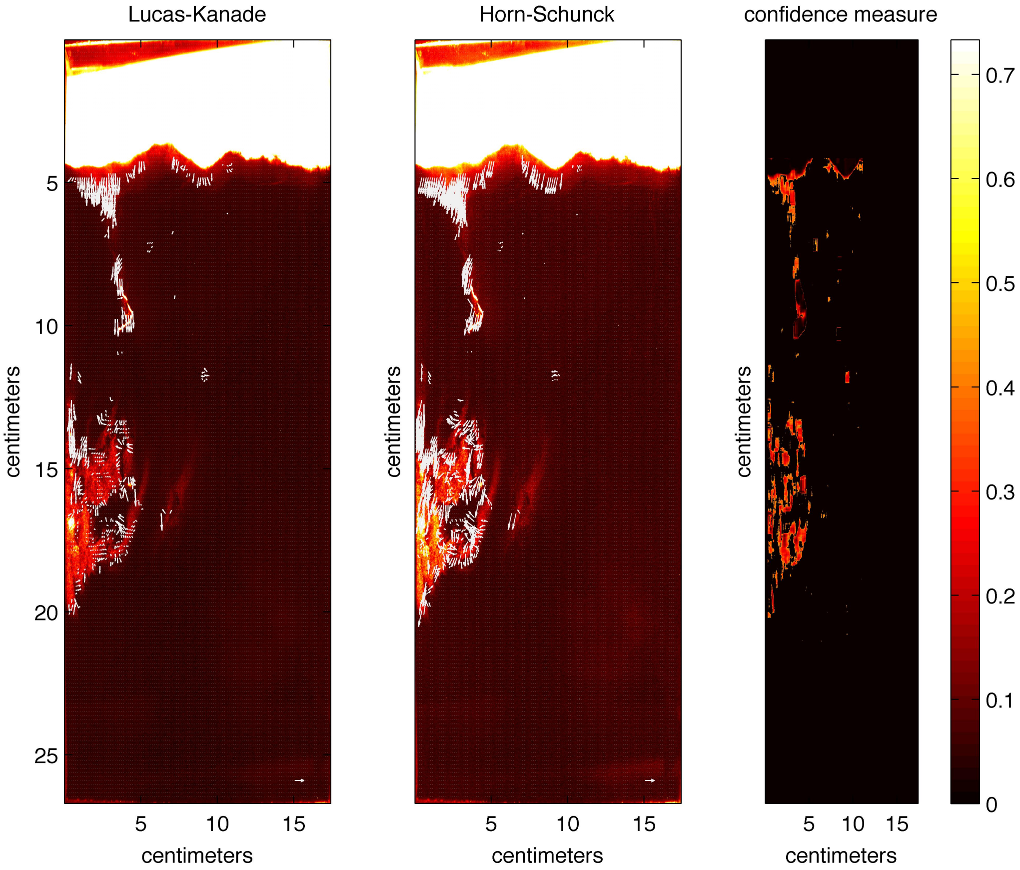

Figure 28 The optical flow velocities obtained using HS and LK methods are plotted on the images (real images taken on 2nd november) used to calculate the optical flow. Bright color in the two left panels denotes high tracer concentration, most evident in the overlying water. The confidence measure (right panel, with color bar) shows the region where we have actual information in warmer colors and represents different domain, as it is not extended into water. The flow in the regions where the confidence measure is high is considered as reliable flow. For the LK and HS methods the reference arrow located at (15,25) is of the length $2*10^{-4}$cm/s

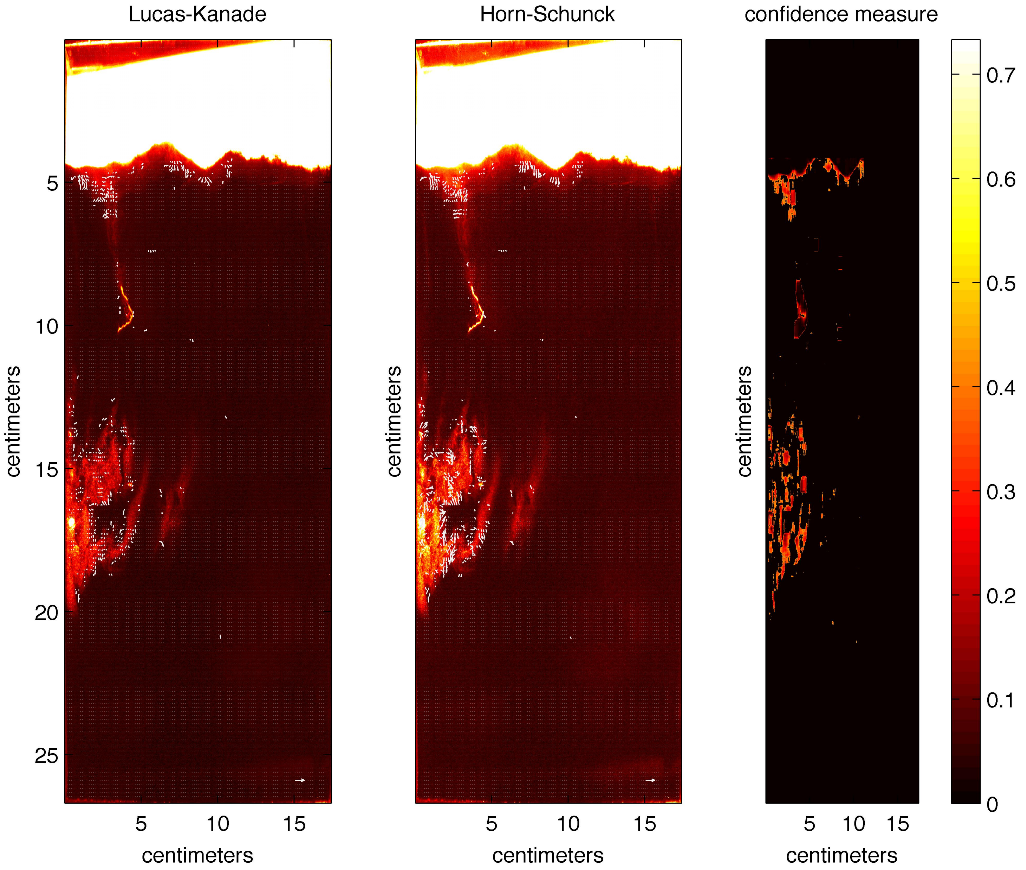

Figure 29 As Figure 25, but for a different timeslice.

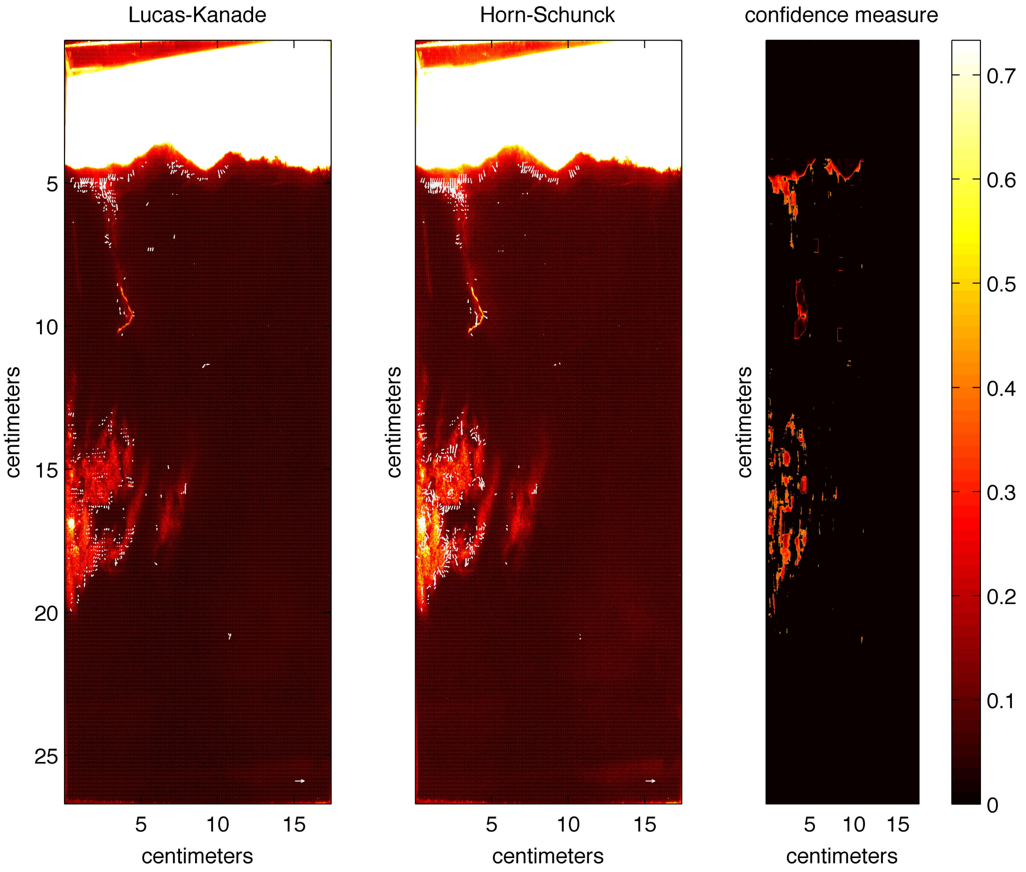

Figure 30 As Figure 25, but for a different timeslice.

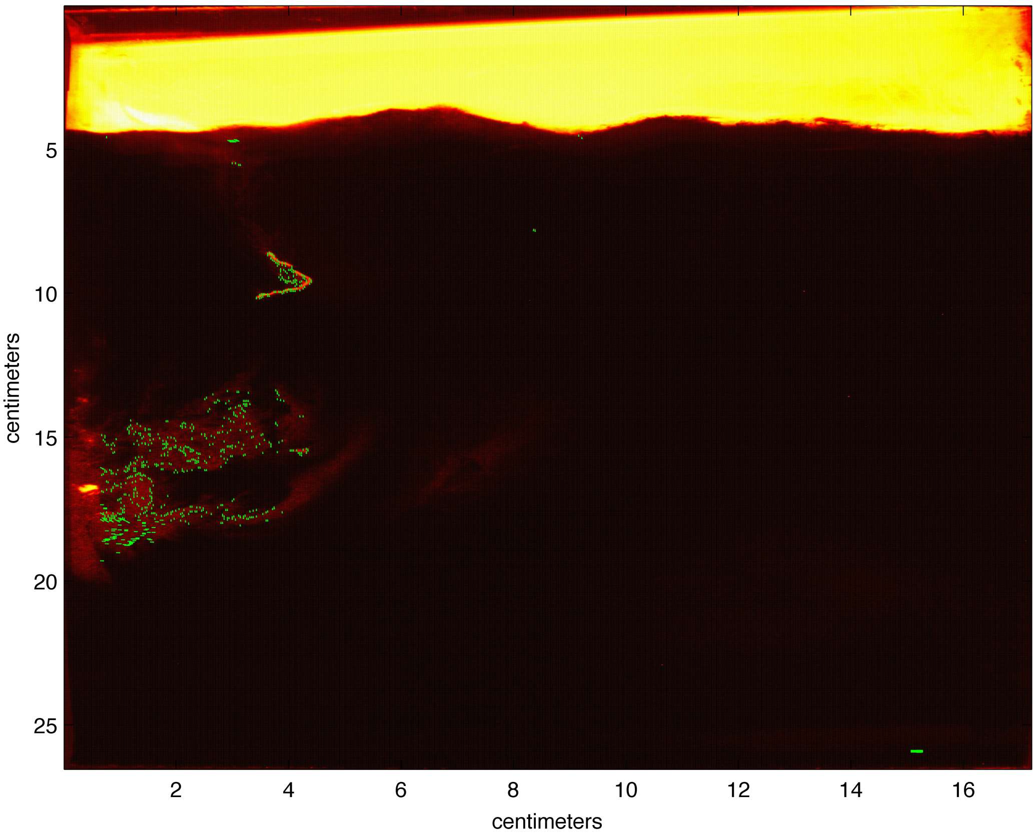

Figure 31 The optical flow velocities obtained using edge tracking methods are plotted on the images (real images taken on 2nd November) used to calculate the optical flow. The confidence measure shows the region where we have actual information. The flow in the regions where the confidence measure is high is considered as reliable flow. The reference arrow located at (15,25) is of the magnitude 5*10^{-4}cm/s

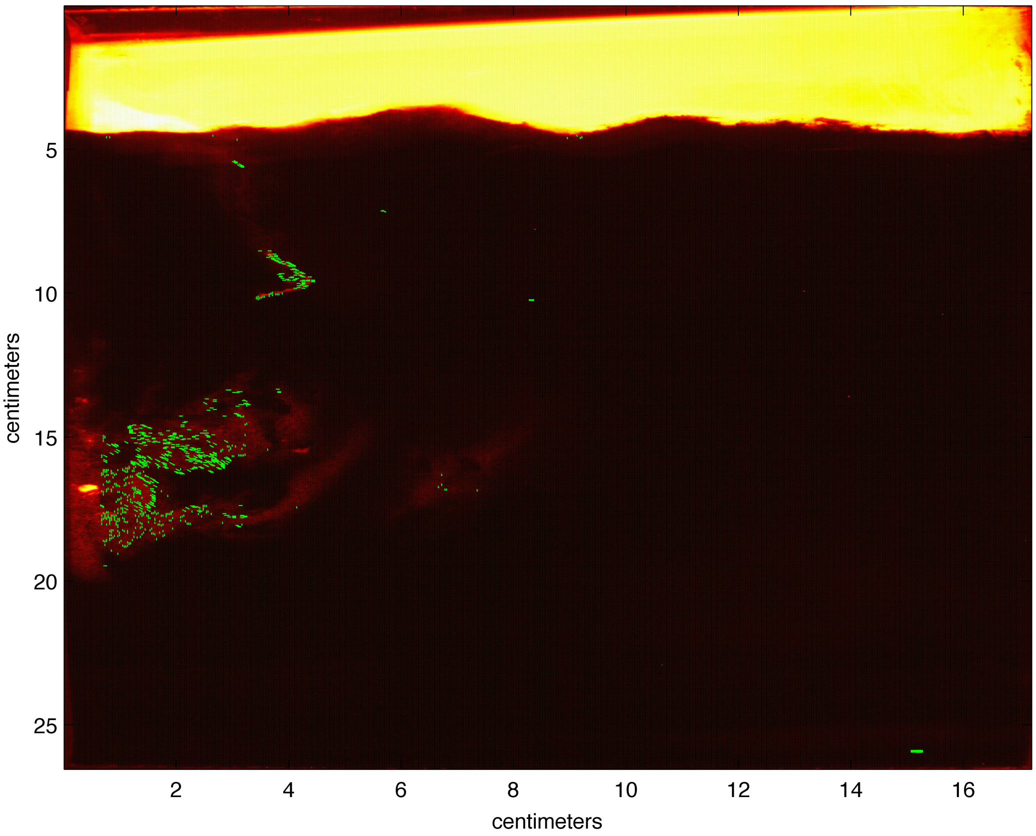

Figure 32 As Figure 28, but for a different timeslice.

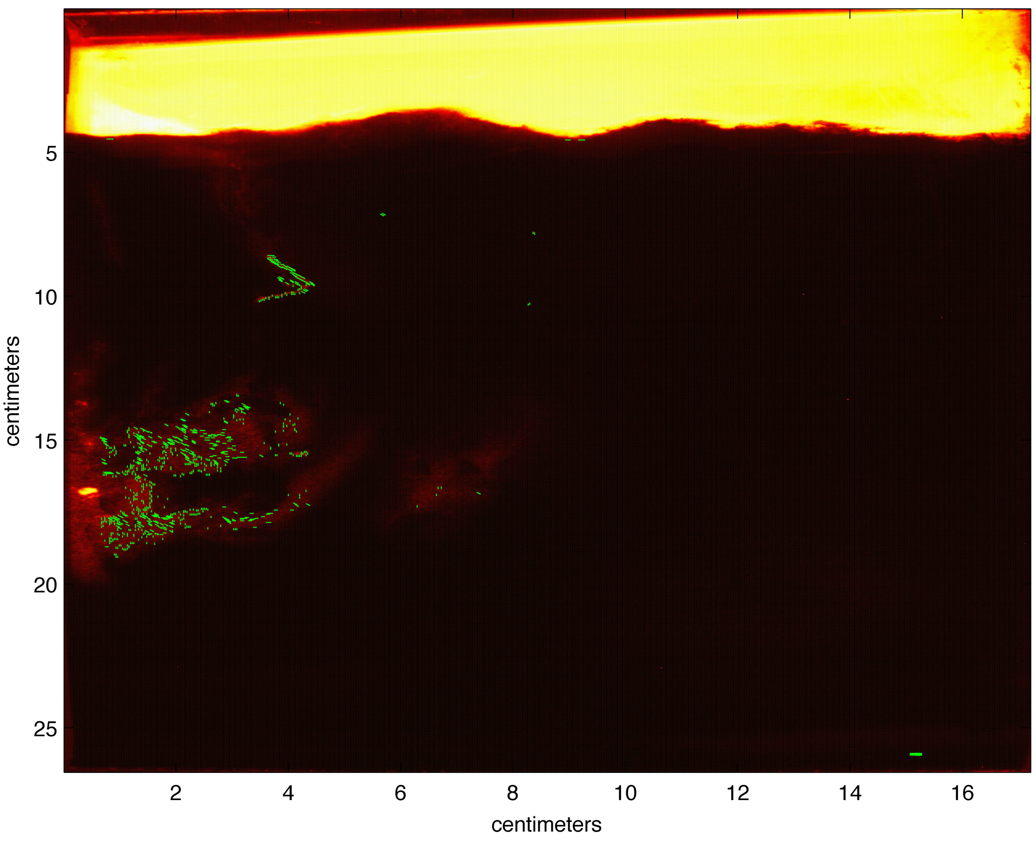

Figure 33 As Figure 28, but for a different timeslice.

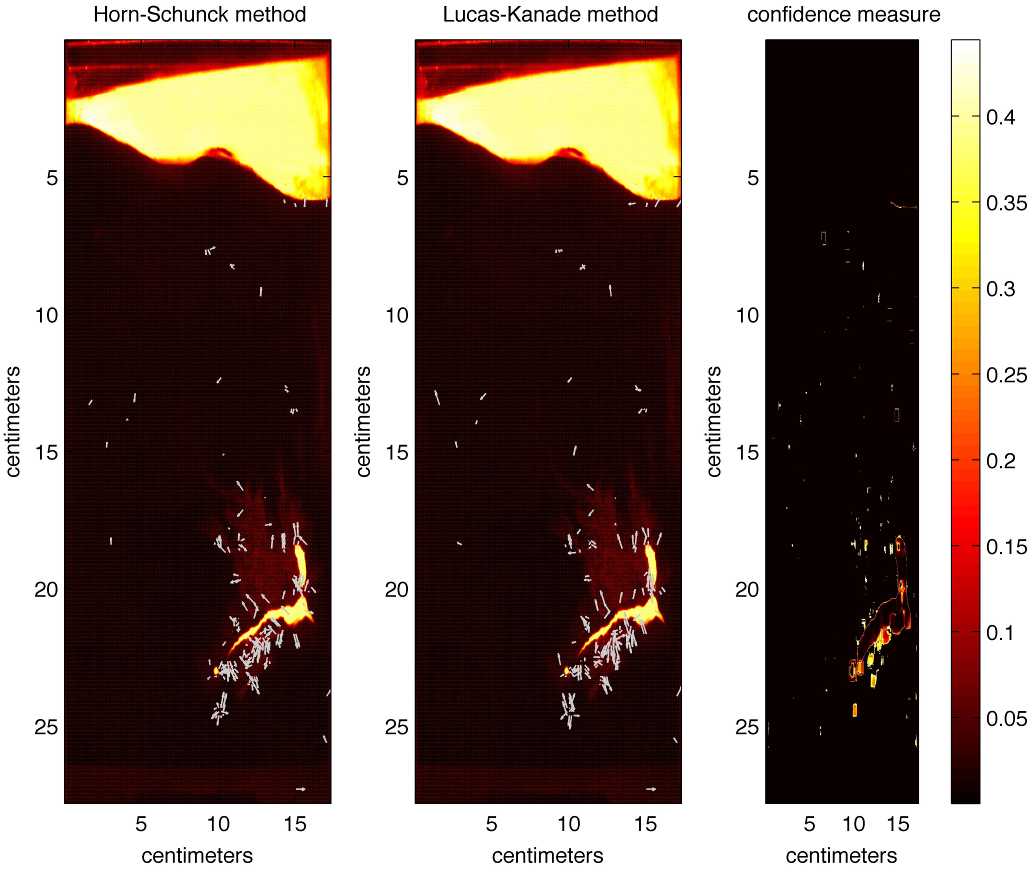

Figure 34 The optical flow velocities obtained using HS and LK methods are plotted on the images (real images taken on 28th June) used to calculate the optical flow. The confidence measure shows the region where we have actual information. The flow in the regions where the confidence measure is high is considered as reliable flow. The reference arrow located at (15,25) is of the magnitude 10^{-4}cm/s

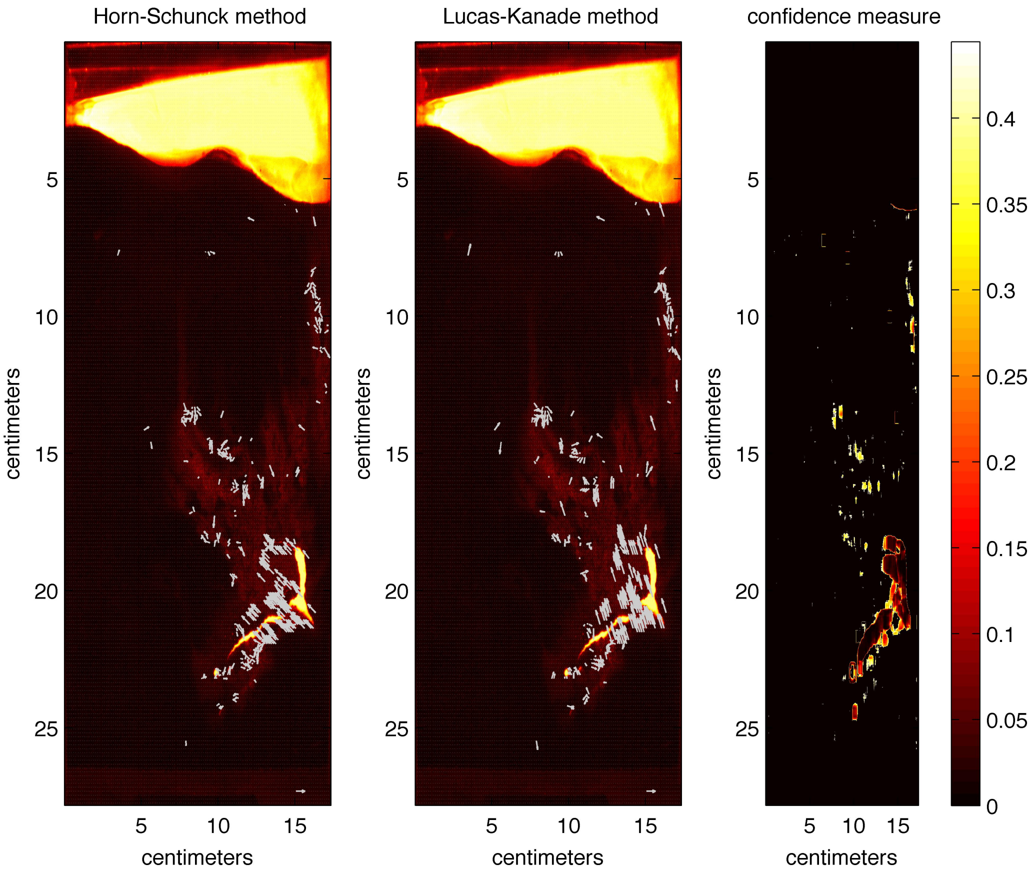

Figure 35 As Figure 31, but for a different timeslice.

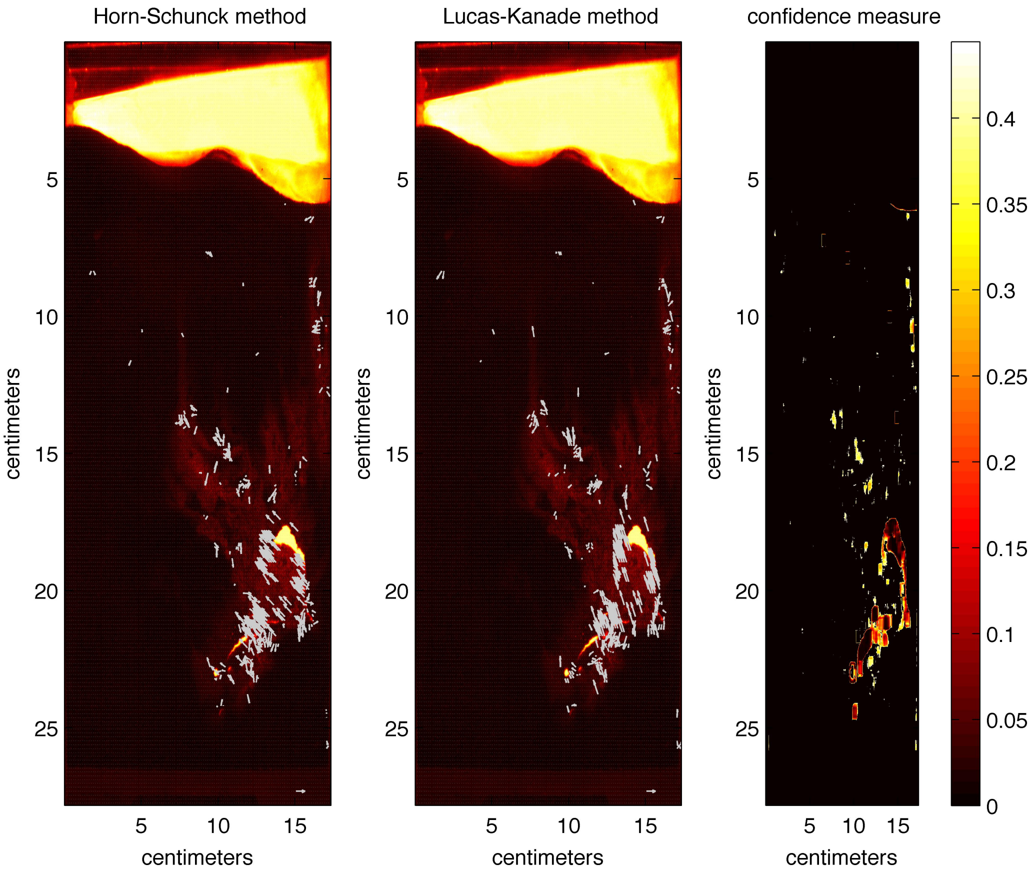

Figure 36 As Figure 31, but for a different timeslice.

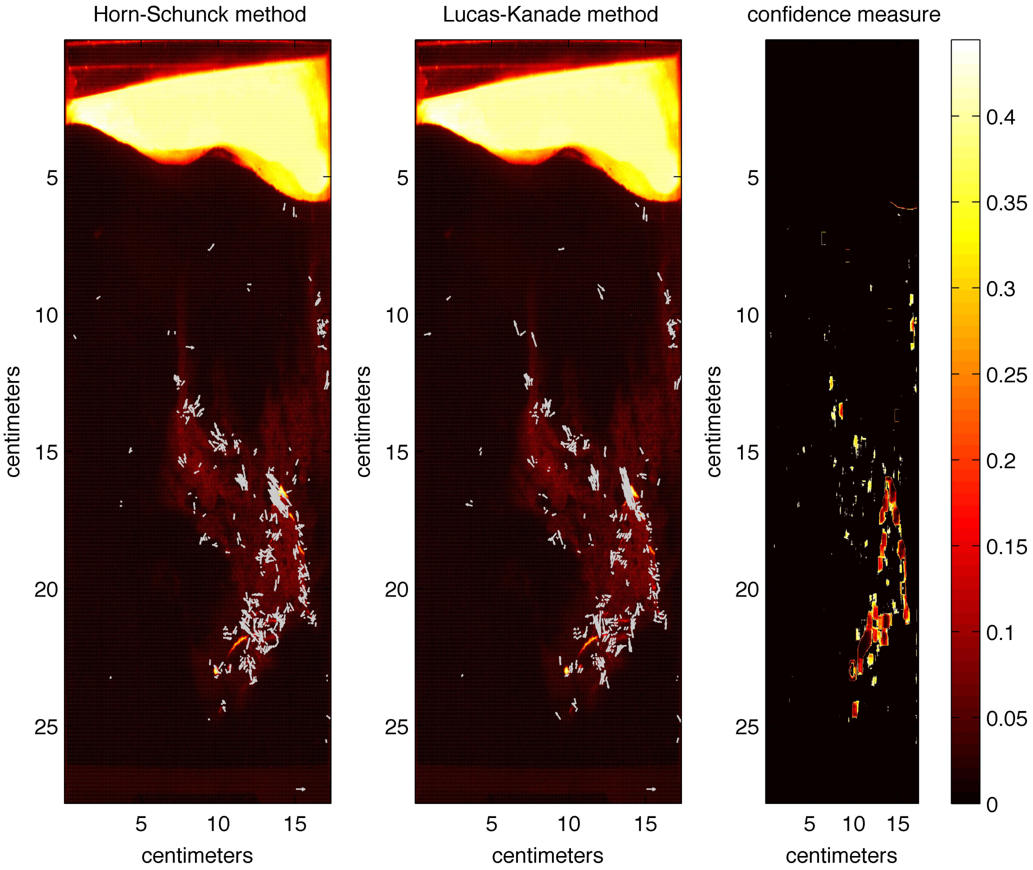

Figure 37 As Figure 31, but for a different timeslice.

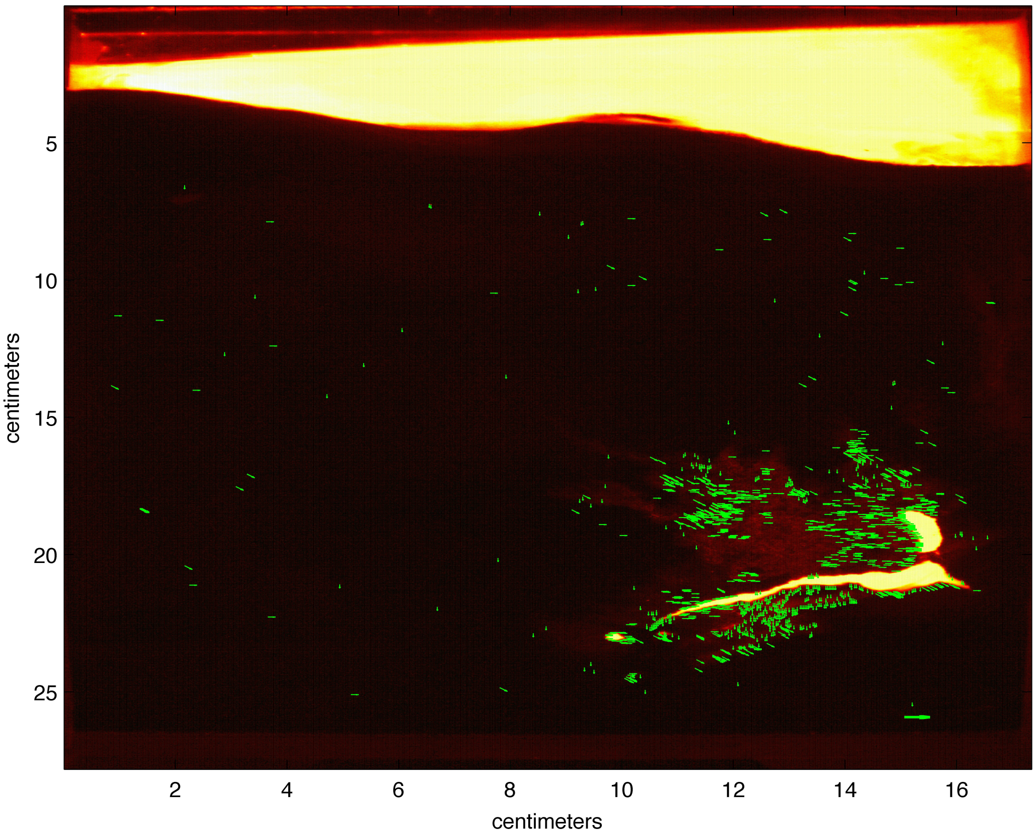

Figure 38 The optical flow velocities obtained using HS and LK methods are plotted on the images (real images taken on 28th June) used to calculate the optical flow. The confidence measure shows the region where we have actual information. The flow in the regions where the confidence measure is high is considered as reliable flow. The reference arrow located at (15,25) is of the magnitude 10^{-4}cm/s

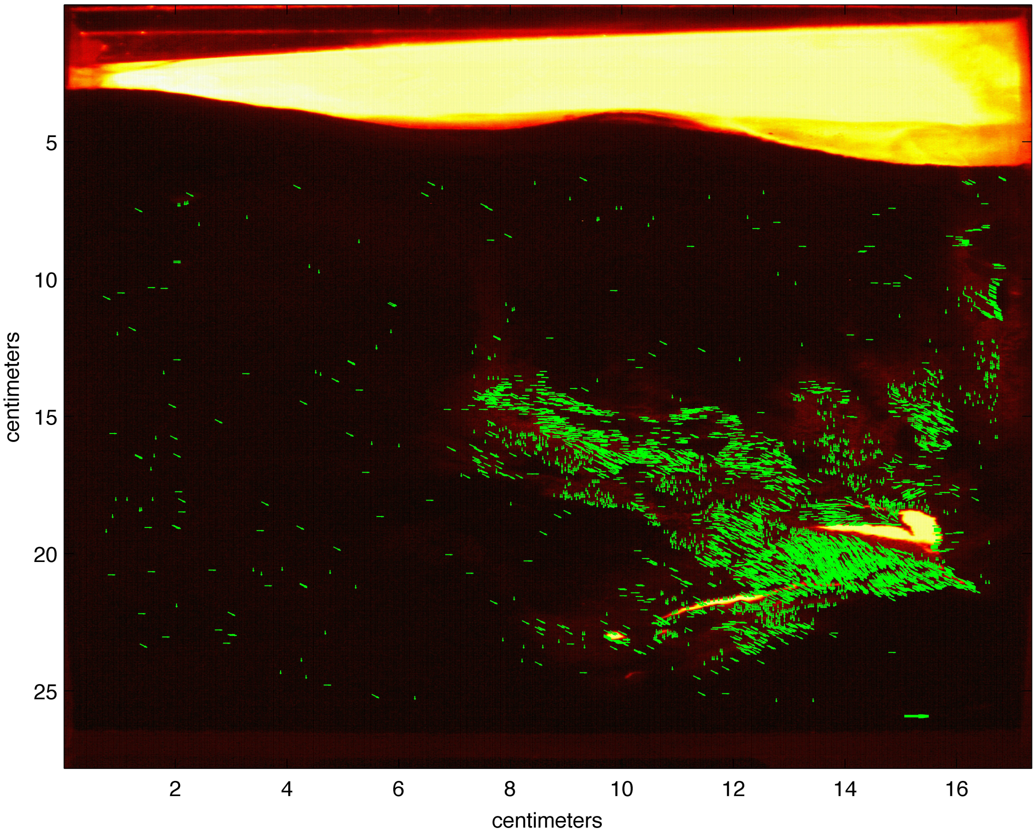

Figure 39 As Figure 35, but for a different timeslice.

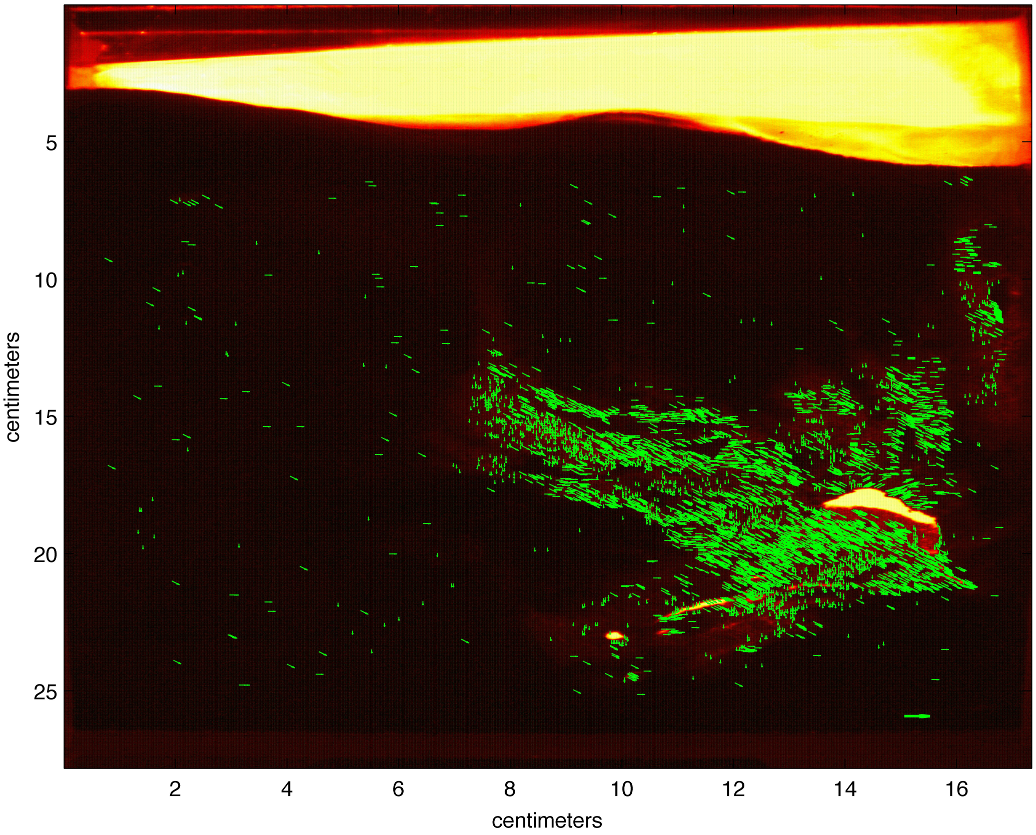

Figure 40 As Figure 35, but for a different timeslice.

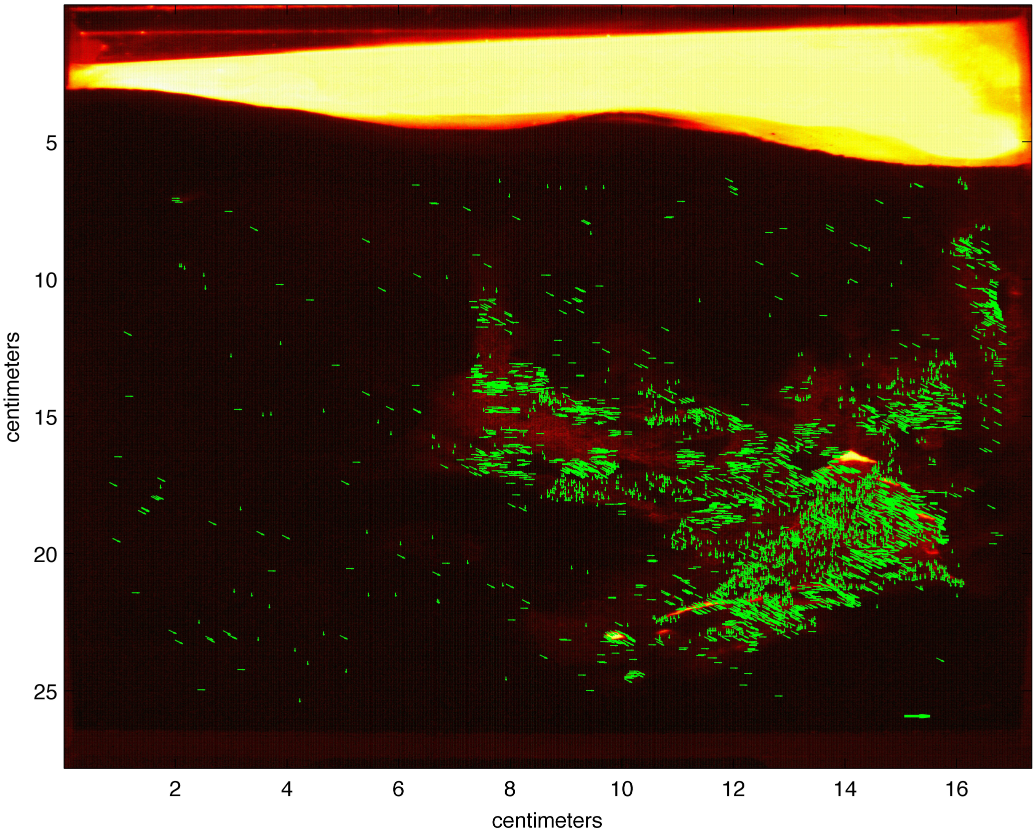

Figure 41 As Figure 35, but for a different timeslice.

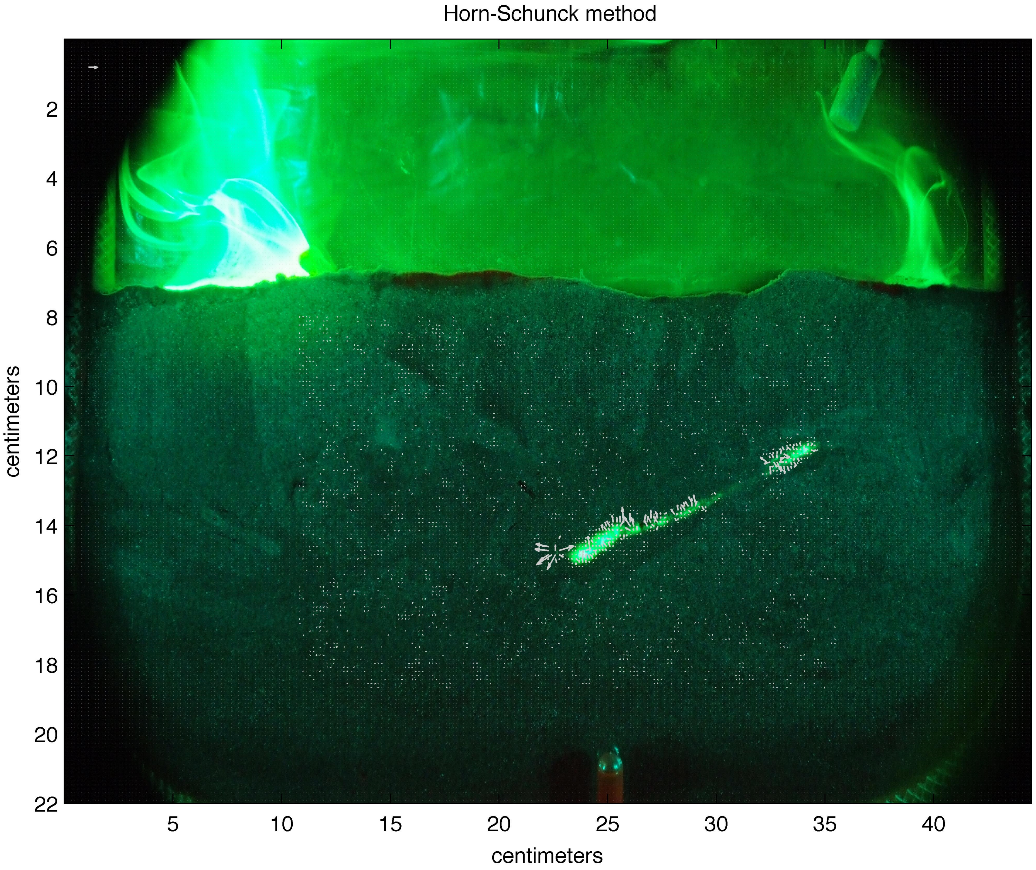

Figure 42 The optical flow a velocity obtained using HS method is plotted on the images (images of experiment2) used to calculate the optical flow. The reference arrow located at (1,3) is of the magnitude 10^{-3}cm/s. The reference arrow is of the magnitude 1e-3cm/s and is located at (2,2).

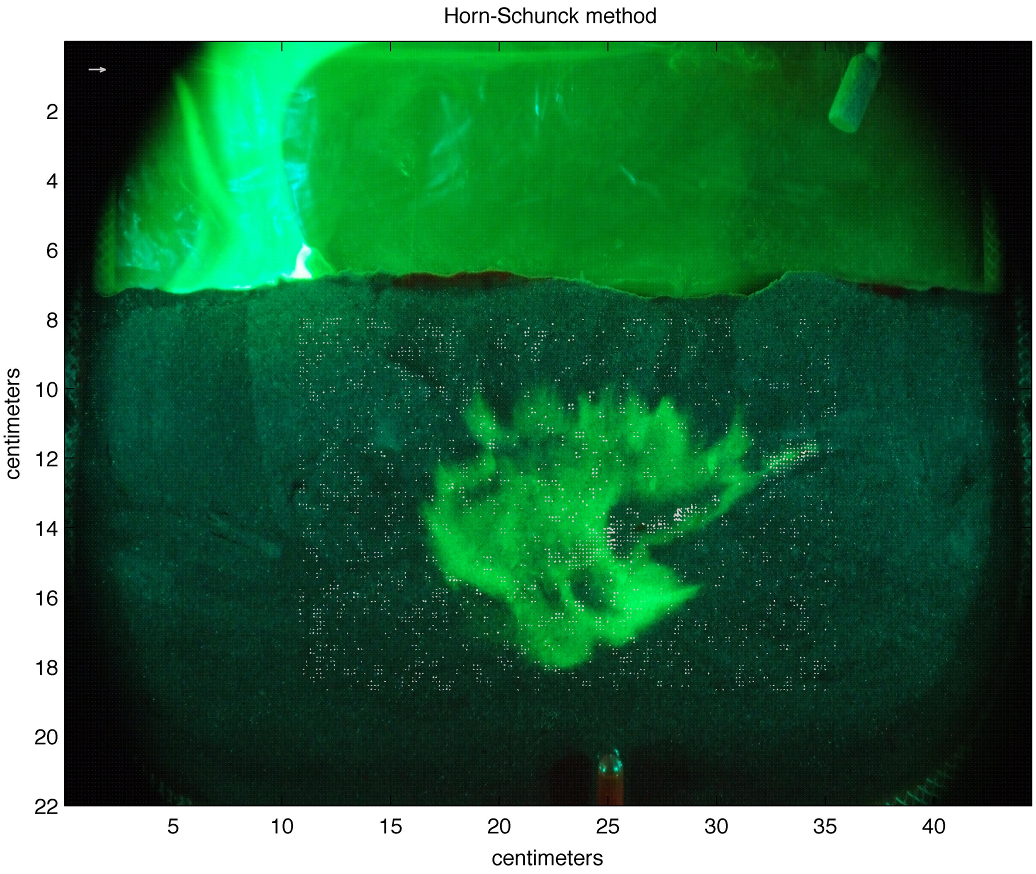

Figure 43 similar to figure 39, but at a different time step

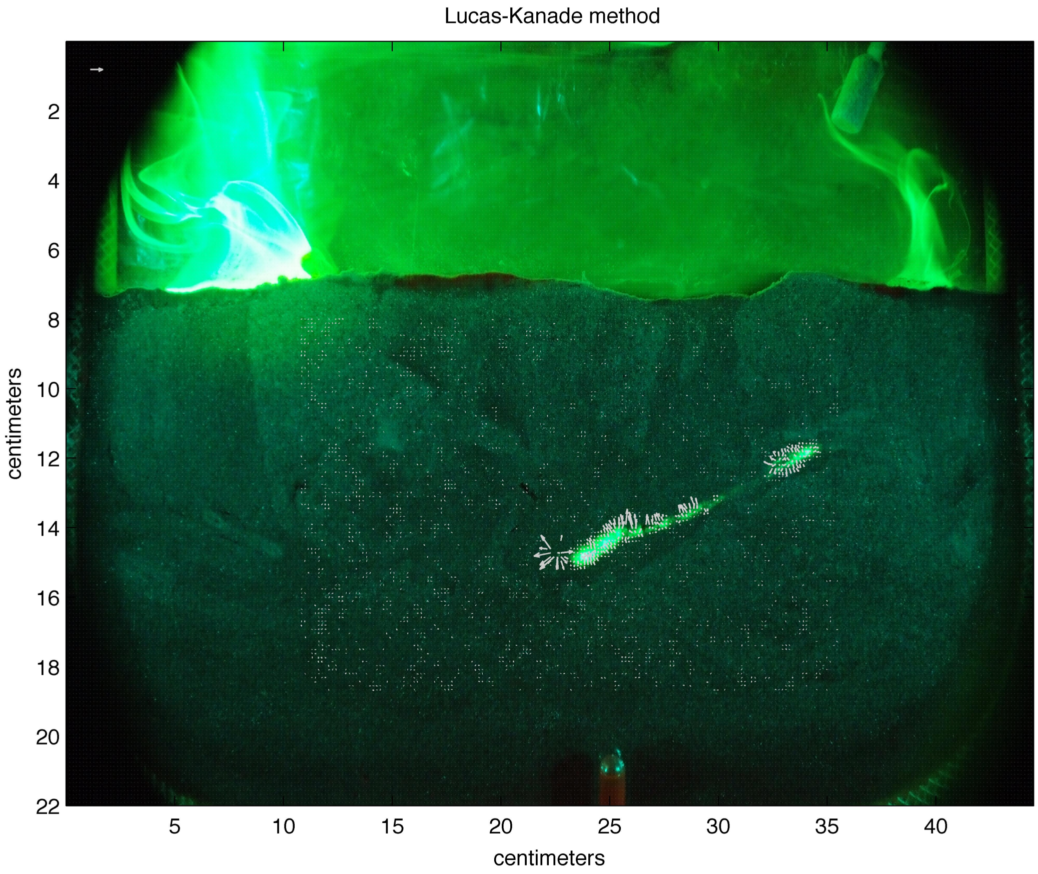

Figure 44 The optical flow a velocity obtained using LK method is plotted on the images (images of experiment2) used to calculate the optical flow. The reference arrow located at (1,3) is of the magnitude 10^{-3}cm/s

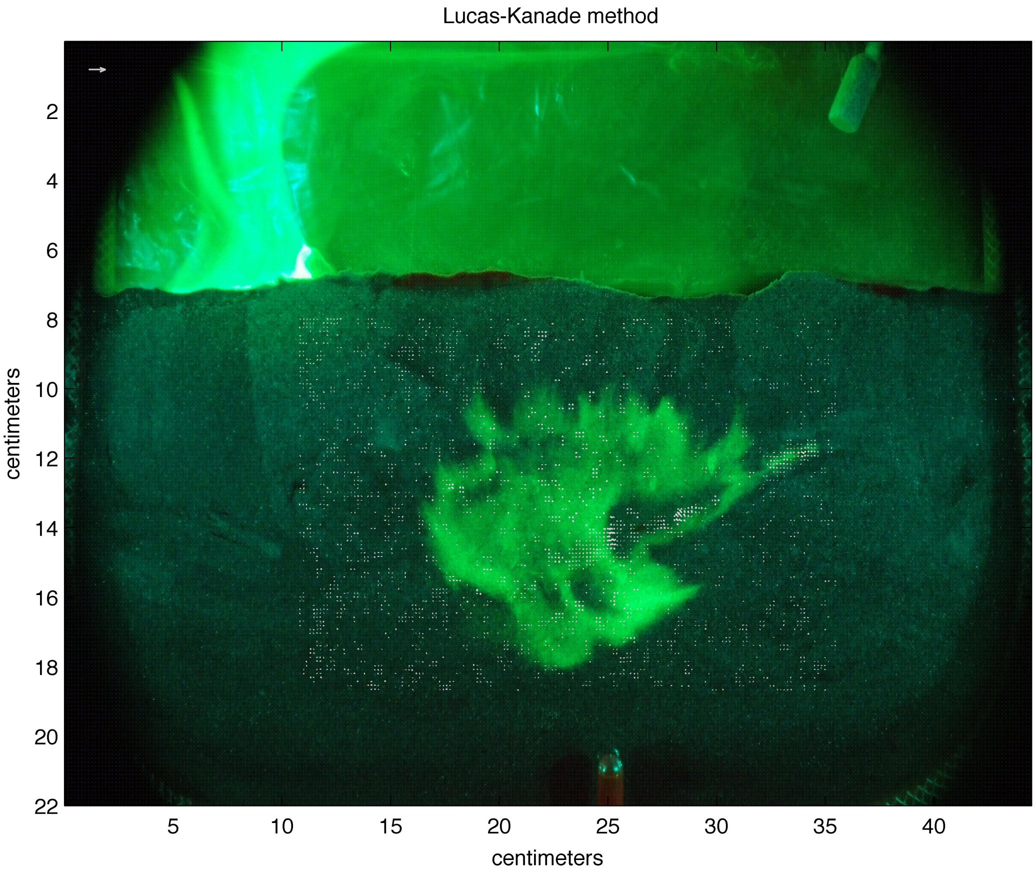

Figure 45 similar to figure 42, but at a different time step

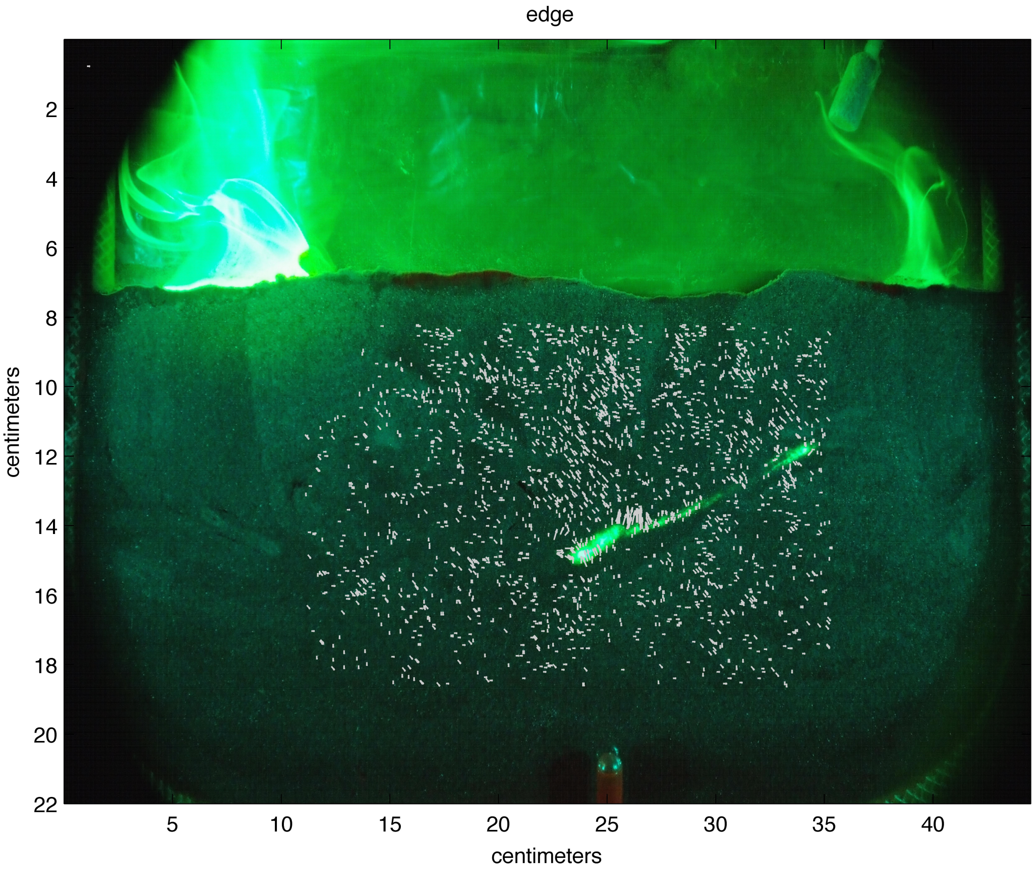

Figure 46 The optical flow a velocity obtained using edge tracking method is plotted on the images (images of experiment2) used to calculate the optical flow. The reference arrow located at (1,3) is of the magnitude 10^{-2}cm/s. The reference arrow is of the magnitude 1e-3cm/s and is located at (2,2).

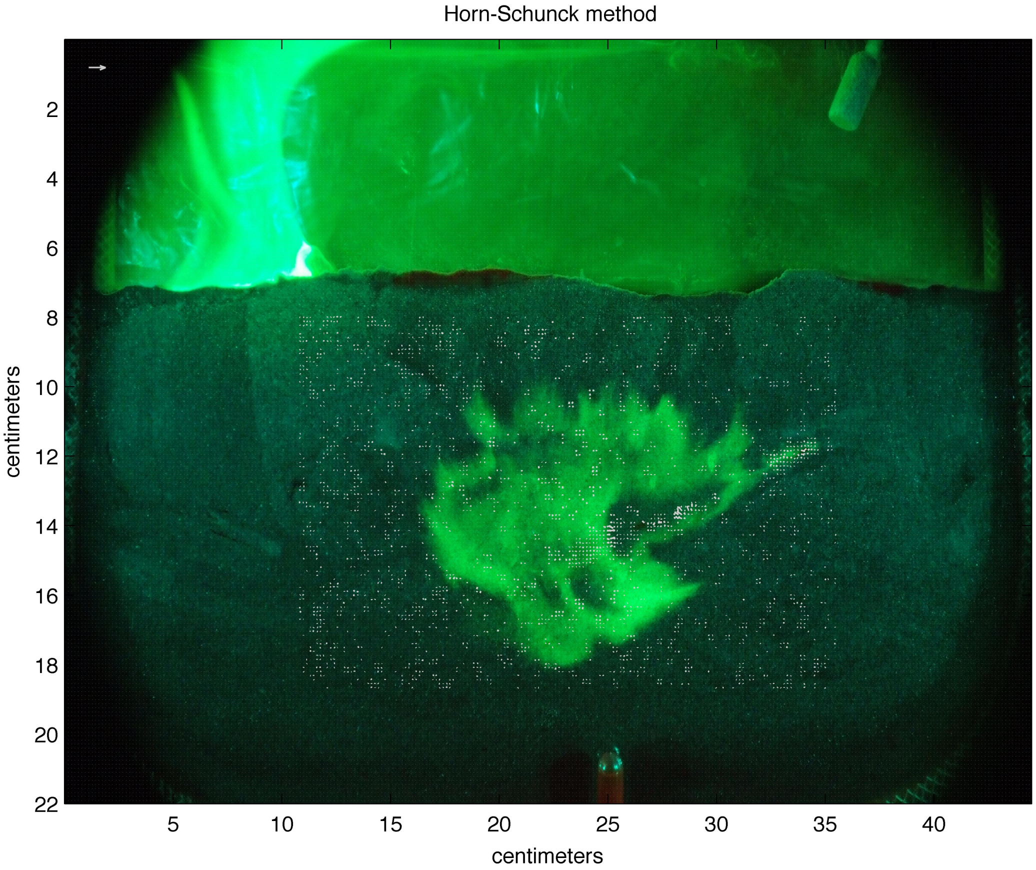

Figure 47 same as figure 43, at a different time step.